CrossMark

J. Fluid Mech. (2018), *vol.* 846, *pp.* 508–535. © Cambridge University Press 2018
doi:10.1017/jfm.2018.273

Dynamics of water entry

Lionel Vincent[1], Tingben Xiao[1], Daniel Yohann[1], Sunghwan Jung[2] and Eva Kanso[1,†]

[1]Aerospace and Mechanical Engineering, University of Southern California, Los Angeles, CA 90089, USA

[2]Department of Biomedical Engineering and Mechanics, Virginia Tech, Blacksburg, VA 24060, USA

(Received 28 July 2017; revised 3 January 2018; accepted 20 March 2018; first published online 10 May 2018)

Diving induces large pressure during water entry accompanied by the creation of cavity and water splash ejected from the free water surface. To minimize impact forces, divers streamline their shape at impact. Here, we investigate the impact forces and splash evolution of wedges entering water as a function of the wedge opening angle. A gradual transition from impactful to smooth entry is observed as the wedge angle decreases. After submersion, the wedge experiences significantly smaller drag forces (two-fold smaller) than immersed wedges. Our experimental findings compare favourably with existing force models upon the introduction of empirically based corrections. We experimentally characterize the shapes of the cavity and splash created by the wedge and find that they are independent of the entry velocity at short times, but that the splash exhibits distinct variations in shape at later times. We propose a one-dimensional model of the splash that takes into account gravity, surface tension and aerodynamic forces. The model shows, in conjunction with experimental data, that the splash shape is dominated by the interplay between a destabilizing Venturi-suction force due to air rushing between the splash and the water surface and a stabilizing force due to surface tension. Taken together, these findings could direct future research aimed at understanding and combining the mechanisms underlying all stages of water entry in application to engineering and bio-related problems, including naval engineering, disease spreading or platform diving.

Key words: flow–structure interactions, jets, thin films

1. Introduction

We investigate the motion of a rigid wedge diving across an air–water interface. Water entry problems have appealed to scientists and engineers alike for more than a century. The beauty of splashes was first examined using high-speed photography by Worthington (1908) and later studied in the context of naval engineering problems (Von Kármán 1929; Wagner 1932). While naval-oriented research is still very active (Abrate 2011), understanding and predicting forces on entering objects is also relevant for other fields, such as air–water missiles (May 1952), aerospace engineering (Seddon & Moatamedi 2006), diving birds (Ropert-Coudert *et al.* 1994; Chang *et al.* 2016) and

†Email address for correspondence: kanso@usc.edu

https://doi.org/10.1017/jfm.2018.273 Published online by Cambridge University Press

lizard locomotion (Hsieh & Lauder 2004), as well as prevention of injury in Olympic diving (Harrison *et al.* 2012) and dissemination of seeds (Amador *et al.* 2013), aroma (Ghabache *et al.* 2014) and diseases (Gilet & Bourouiba 2015; Joung, Ge & Buie 2017).

In this study, wedges of width d and opening angle α are dropped under gravity g from a height H, as shown in figure 1(*a*). They reach the air–water interface with a velocity $V \approx \sqrt{2gH}$. Figure 1(*b*) shows the stages of water entry and corresponding vertical force acting on the supporting arm of a wedge of width $d = 18$ mm and entry velocity $V = 1.70$ m s^{-1}. This sequence illustrates several generic features of water entry. Shortly after first contact with the water surface, the vertical force quickly rises from 0 to a peak value; labels (B–C) in figure 1(*b*). The peak is very prominent and is reached before the wedge is completely submerged. This characteristic pattern is called 'slamming'. The vertical force then decreases (C–D) and changes little once the wedge is fully submerged (D–E). Following submersion (D–E–F), two visually striking events occur. First, an air-filled expanding cavity is created in the wedge's wake. Second, a curved splash is ejected upwards and sideways from the point of impact. The ejection velocity can be significantly higher than the wedge's entry velocity V: the thin and fast-moving splash is subject to aerodynamic interactions leading to non-trivial arabesques (E). This work is focused on the description and modelling of the vertical force generated during entry, as well as modelling the splash sheet kinematics. The first part deals with early stages of water entry (prior to the wedge's total submersion), and in particular the transition from smooth to impactful entry as the wedge angle increases. The second part analyses, using a combination of empirical observations and low-order physics-based models, the long-term evolution of the splash projected upwards from the edges of the wedge during and following water entry.

1.1. *Impact forces on objects entering water*

The fluid dynamics literature is divided into two types: those that focus on forces during impact, and others that focus on the cavity and splash formation. Von Kármán (1929) was the first to estimate the slamming forces on wedges based on conservation of fluid-wedge momentum and the added mass effect. Shortly after, Wagner (1932) presented a model based on potential flow theory, in which free surface elevation was taken into account. Potential flow models are relevant (i) for analysing large impact velocities where viscous effects are negligible and (ii) for solving for the flow on the leading part of the wedge (not past it), on which a vorticity-free flow is expected (see, for example, Park & Rhee 2012). Most current models of the impact force during water entry are refinements of Wagner's original work. Wagner's original model provides good predictions of the impact force for nearly flat wedges ($\alpha \approx 180°$), but leads to large overestimates at moderate opening angles (close to a two-fold error for $\alpha = 120°$: see Korobkin (2004)). Perhaps the most celebrated model among the improved derivations is the one of Logvinovich (1972), which provides an accurate description of the maximum impact force and correctly predicts the pressure distribution on the wedge's wetted surface; for more details, see Korobkin (2004) and Panciroli, Shams & Porfiri (2015). Zhao & Faltinsen (1993) and Zhao, Faltinsen & Aarsnes (1996) were the first to propose a fully nonlinear solution for the coupled fluid-wedge system, and Mei, Liu & Yue (1999) developed a conformal mapping technique that built upon these findings. In a series of publications (Korobkin & Pukhnachov 1988; Korobkin 1996, 2001, 2004), Korobkin offered a

https://doi.org/10.1017/jfm.2018.273 Published online by Cambridge University Press

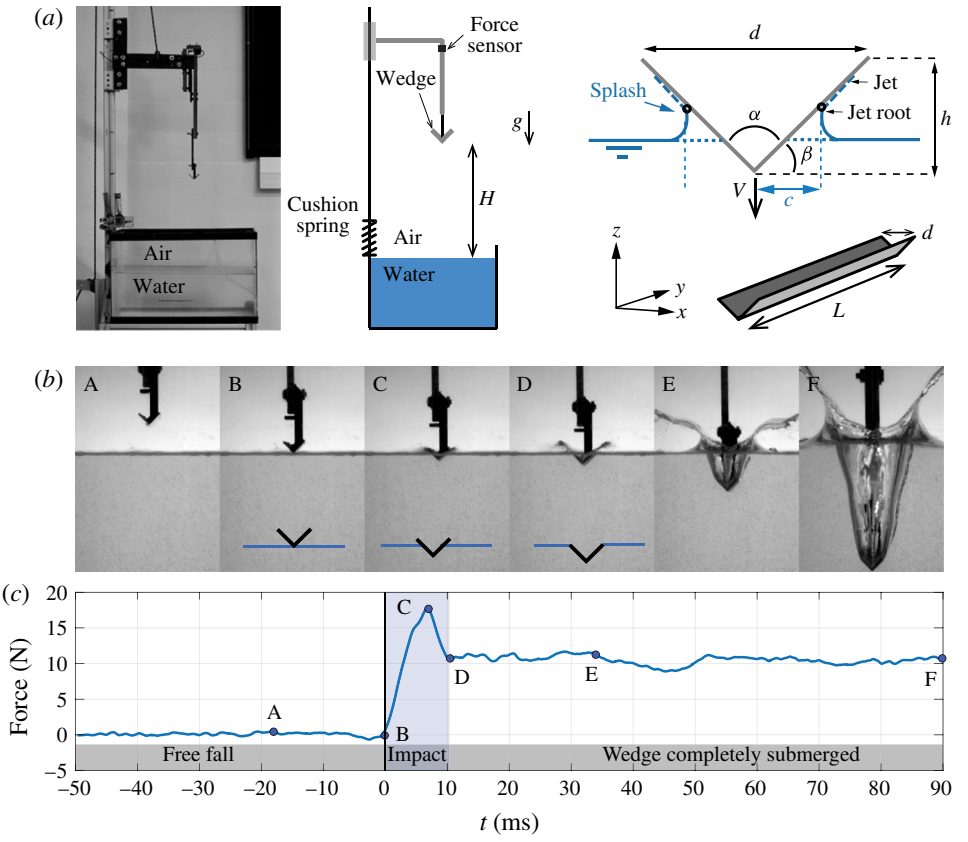


FIGURE 1. (Colour online) (*a*) Experimental set-up. 3D-printed wedges of length L, width d and opening angle α are attached to a vertical heavy slider and dropped from a height H; they hit the air–water interface with a velocity $V \approx \sqrt{2gH}$. Alternatively, the wedge is defined by the deadrise angle $\beta = (\pi - \alpha)/2$ and $h = (d/2)\tan\beta$. As the wedge dives, water piles up underneath the wedge, and a jet is formed. c designates the time-dependent horizontal location of the jet root. A force sensor mounted on the supporting arm measures the compression force during entry. (*b*,*c*) Typical water entry sequence and force measurement for an $\alpha = 90°$ wedge of $d = 18$ mm impacting at $V = 1.70$ m s^{-1}. For large enough wedge angles ($\alpha > 70°$), the compression force peaks before the wedge is fully submerged; a smaller, quasi-constant force is observed after complete submersion. $t = 0$ is defined as the first contact between the wedge and the water surface. The entry generates a thin and fast-moving splash, likely to interact with the surrounding air.

number of insightful analytical models of fluid entry under various conditions. Explicit finite-element methods have been employed by Bereznitski (2001), Stenius, Rosen & Kuttenkeuler (2006), Wang, Luo & Soares (2012) and Calderer, Kans & Sotiropoulos (2014) to predict slamming loads. While many theoretical and numerical models predict impact forces on wedges of relatively small angles, there are few experimental studies that seek to validate these predictions (Zhao *et al.* 1996; Wu, Sun & He 2004; Yettou, Desrochers & Champoux 2006; Tveitnes, Fairlie-Clarke & Varyani 2008). Even fewer studies consider and quantify the unavoidable three-dimensional effects of real-life experiments (Zhao *et al.* 1996).

https://doi.org/10.1017/jfm.2018.273 Published online by Cambridge University Press

After the wedge is submerged, the presence of the cavity affects the hydrodynamic drag force. The flow past an object with a trailing cavity is expected to be more streamlined than past a fully immersed object. In the latter, vorticity, recirculation and turbulence are expected downstream of the object, angled or not (see, for instance, Rosenhead (1939), Moffat (1964) and Truscott, Epps & Techet (2012)). Experimental measurements on spheres and disks entering water have shown that the drag coefficient is reduced by half when compared to the fully immersed case (May & Woodhull 1948; Glasheen & McMahon 1996). There is, to our knowledge, no systematic model of how transient cavities affect drag on translating wedges. However, results about the influence of supercavities (induced by cavitation) on drag are available and show that the drag coefficient can be expressed as a function of the shape of the steady trailing cavity (Knapp, Daily & Hammitt 1970). We will tentatively apply these results to the transient (inertial) cavity generated by water entry, keeping in mind the physical origin of the cavity is different.

In the first part of this paper, we characterize the forces acting on the wedge during water entry (before and after submersion), and we compare our experimental results to existing theories. We show that wedges with large angles undergo 'impactful' entry, characterized by the presence of a large peak force before submersion. In contrast, low-angle wedges enter smoothly, with a force gradually rising from zero to a terminal value. We demonstrate that the transition between impactful and smooth entry can be predicted using Logvinovich's model. We also show that the drag force acting on the wedge after submersion is quasi-constant and, because of the presence of the cavity, it is significantly lower than the drag force of an immersed wedge.

1.2. *Splash and cavity evolution*

The study of splashes and cavities dates back to the beginning of high-speed photography (Worthington 1908) and continues to be the topic of numerous publications (Birkhoff & Zarantonello 1957; Duclaux *et al.* 2007; Aristoff & Bush 2009). Most studies consider either the dynamics of the cavity or the development of the splash. An air cavity evolves relatively slowly with respect to the object's velocity and is thus easier to visualize and analyse. The retroaction of the cavity dynamics on the trajectory of the impacting object is of interest for the military, for directing bullets or air–water anti-torpedo missiles towards an underwater target (May 1952; Birkhoff & Zarantonello 1957). At very large impact velocities, the low-pressure area in the object's wake triggers cavitation (Truscott, Epps & Belden 2014), which affects the stability of the object's trajectory. At slower impact velocity, the cavity is primarily the result of inertia. Many research contributions focus on describing, classifying and modelling the cavity created by various impactors (Duclaux *et al.* 2007; Aristoff & Bush 2009; Truscott & Techet 2009; Marston *et al.* 2016). Splashes, in contrast, are thin and fast-developing features of elusive nature. Unlike cavities, they are strongly dependent on the geometry of the object. Splashes have been extensively studied in the canonical problem of impacting spheres. Water entry of spheres is usually accompanied by a nearly vertical splash curtain (Worthington 1908; Aristoff & Bush 2009). Entry of wedges, because of the large horizontal momentum imparted to the liquid, generally induces splashes curving outwards and downwards (Greenhow 1987). These splashes are generally better defined, thicker, and less sensitive to wettability than splashes created by round objects, but they are considerably less studied than the latter.

For splashes, perhaps more than for any other aspects of water entry, the devil is in the details. Classically, water entry has been thought of as a problem driven by

https://doi.org/10.1017/jfm.2018.273 Published online by Cambridge University Press

inertia for sufficiently high entry velocities. As Duez *et al.* (2007) pointed out, this view is essentially wrong. They demonstrated that capillary effects such as wettability have first-order effects on the cavity formation and subsequent splashes for spheres. Likewise, Marston *et al.* (2016) showed that capillary wrinkles originating from the contact line on the sphere are responsible for the dramatic splash shape upon 'buckling'. Viscosity is also usually neglected, even though we can expect that for very thin fluid structures such as splashes, its effect could become important. Lastly, the surrounding air affects various aspects of the splash, including the ejecta (Quéré 2005; Xu, Zhang & Nagel 2005), cavity collapse in axisymmetric problems (Gordillo *et al.* 2005; Gekle *et al.* 2010) and quasi-two-dimensional problems (Wang, Lugni & Faltinsen 2015), and surface seal (Marston *et al.* 2015).

Attempts to simulate splashes have been met so far with mixed results, including for simple geometries such as wedges. In early models and simulations, the jet is either not considered at all (Wagner 1932; Logvinovich 1972), or cut off when leaving the wedge to avoid numerical difficulties (Zhao *et al.* 1996; Battistin & Iafrati 2003). Recent contributions use smoothed particle hydrodynamics (Gong, Liu & Wang 2009), level-set immersed boundary methods (Calderer *et al.* 2014) or boundary element methods based on potential flow theory (Wu *et al.* 2004; Bao, Wu & Xu 2016) to solve the full system and account for the free jet. However, most simulations either misrepresent the splash development (Calderer *et al.* 2014) or fail to include potentially important parameters such as surface tension (Bao *et al.* 2016). In short, existing descriptions of the splash shape lack a proper framework to help understand the effects of various physical forces on the splash evolution.

The second part of this study focuses on the cavity and splash evolution created by diving wedges. Using high-speed photography to reconstruct the shapes of the cavity and splash, we show that the cavity is self-similar for various entry velocities but the splash is not. In order to investigate the physics underlying the splash evolution, we develop a one-dimensional model based on the idea that the splash is primarily ballistic, and can be represented by a succession of discrete particles ejected from the free water surface. Our model bears similarity to previous models developed in the context of a moving fluid sheet (Gart *et al.* 2013), but it goes further in that it takes into account the sheet stretching and original contributions such as aerodynamic suction forces. The model shows, in conjunction with the experimental data, that the splash shape is the result of the interplay between aerodynamic interactions that favour bending and capillary effects that tend to cancel curvature.

2. Experimental set-up

Wedges were driven by gravity from a height H to enter a water-filled rectangular acrylic tank measuring $51 \times 26 \times 32$ cm^3. To ensure straight and reproducible entry conditions, a vertical tower 1.5 m in height was used to guide the falling wedge; see figure 1(*a*). A wedge dropped from a height $H \leqslant 1.5$ m reaches the air–water interface with a velocity $V \approx \sqrt{2gH} \leqslant 3.5$ m s^{-1}.

The wedges were 3D-printed using Hatchbox PLA plastic of dimensional accuracy ± 0.05 mm. We designed two sets of wedges: (i) we varied the opening angle α from 60° to 120° while maintaining constant wedge width $d = 36$ mm and length $L = 150$ mm (aspect ratio $L/d = 4.2$) and (ii) we varied the projected area $L \times d$ from 1400 to 5940 mm^2 while maintaining constant aspect ratio $L/d = 4.6$ and $\alpha = 90°$. Additionally, we used 90° wedges of a smaller width $d = 18$ mm but the same aspect ratio $L/d = 4.2$ to check that several quantities were independent of d. The mass of

https://doi.org/10.1017/jfm.2018.273 Published online by Cambridge University Press

all moving parts M consisting of the wedge and drop mechanism was approximately 875 g, with the mass of the wedge itself ranging between 15 g and 30 g. The weight Mg was chosen so that it balances the average drag and impact forces during water entry, thus limiting acceleration or deceleration during water entry and allowing us to treat the velocity V of the wedge as constant during water entry.

The water impact problem can be described by three non-dimensional parameters: the Weber number $We = \rho d V^2/\sigma$, where $\rho = 1000$ Kg m^{-3} is the water density and $\sigma = 70 \times 10^{-3}$ N m^{-1} is the surface tension of the air–water interface, the Froude number $Fr = V/\sqrt{gd}$, where $g = 9.81$ m s^{-2} is the gravitational constant, and the Reynolds number $Re = Vd/\nu$, where $\nu = 10^{-6}$ m^2 s^{-1} is the kinematic viscosity of water. Given the experimental parameters, Weber numbers were in the range 200–2000, indicating fluid inertia should dominate surface tension effects. The Froude number ranged from 1.7 to 5, indicating that hydrostatic effects may have a noticeable contribution after the wedge is fully submerged. Lastly, the Reynolds number ranged between 10^4 and 10^5, indicating that the effect of viscosity is negligible. It is worth noting that the relative influence of gravity with respect to surface tension can also be indicated by the Bond number $Bo = We/Fr^2 = \rho g d^2/\sigma$, whose values fall in the range from 45 to 180, confirming that surface tension is not a major player in the forces acting on the wedge during water entry (but will be important in splash development).

Forces acting on the wedge were measured directly by means of a compression load cell (FC22, Measurement Specialties), secured between the horizontal arm connected to the sliders and the vertical rigid stem on which the wedge is mounted (see figure 1*b*). An NI PCIe 6323 acquisition card was used to read data from the compression sensor at a rate of 8000 Hz. A spring was used to keep the wedge and stem in contact with the sensor during the free fall. The small elastic force from this spring was subtracted from the force measurements.

High-speed photography was used to characterize the development of the water jet and air cavity. Water entries were recorded at frame rates ranging between 1600 frames per second and 9000 frames per second using a Phantom Miro M-110 high-speed camera. A minimum of five videos were obtained for each condition with different wedge angles and dropping heights. For each case, we captured front, side, and angled views.

3. Forces during water entry

We characterize the forces acting on diving wedges before and after submersion, with particular emphasis on the gradual transition from impactful to smooth water entry as the wedge angle decreases.

3.1. *Force measurements*

Figure 2(*a–c*) shows the force evolution recorded by the force sensor for three wedges of opening angles $\alpha = 120°$, $\alpha = 90°$ and $\alpha = 60°$, respectively, and for various entry velocities. As in figure 1(*b*), the force quickly rises from 0 to a positive value after impact. For $\alpha = 120°$ and $\alpha = 90°$, the force peaks after entry, with peak values ranging from 10 N to 40 N, then decreases to a quasi-steady value once the wedge is fully submerged. For $\alpha = 60°$, the force gradually increases from 0 to a terminal value; no prominent peak force is observed. We call the first pattern ‘impactful entry’ and the second ‘smooth entry’.

Given the inertial flow regime ($Re > 10^4$), we scale force by $(\rho S V^2)/2$, where $S = L \times d$ is the projected area of the wedge, and introduce the non-dimensional force

https://doi.org/10.1017/jfm.2018.273 Published online by Cambridge University Press

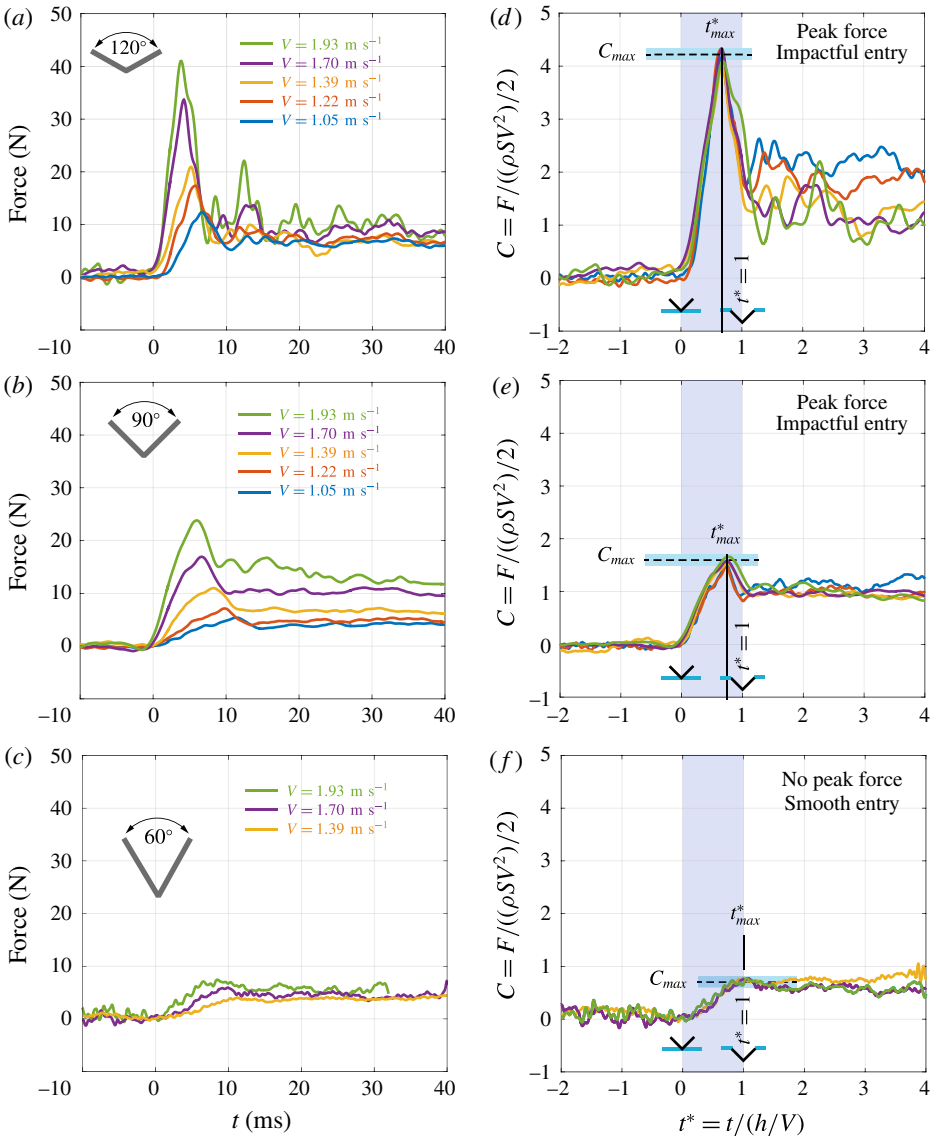


FIGURE 2. (Colour online) Dimensional (*a–c*) and non-dimensional (*d–f*) force history during water entry for 120°, 90° and 60° wedges at various speeds. Note the almost perfect collapse of the force coefficient during the early stages of entry (*d–f*). A prominent peak force appearing for $t^* < 1$ is observed for $\alpha = 120°$ and $\alpha = 90°$, which we define as impactful entry; for smaller angles, such as in (*c*), the measured force gradually rises from $t^* = 0$ (first contact) to $t^* = 1$ (wedge fully submerged): the entry is smooth. $L =$ 150 mm, $d = 36$ mm.

coefficient $C = F/(\rho S V^2)/2$. We also introduce a non-dimensional time $t^* = t/(h/V)$ by scaling time by the inertial time scale h/V, with $t^* = 0$ being the time of impact and $t^* = 1$ corresponding to the instant when the wedge is fully submerged with respect to the undisturbed water surface. The dimensionless force coefficient is depicted in figure 2(*d–f*). For each wedge, the data of different entry velocities collapse for

https://doi.org/10.1017/jfm.2018.273 Published online by Cambridge University Press

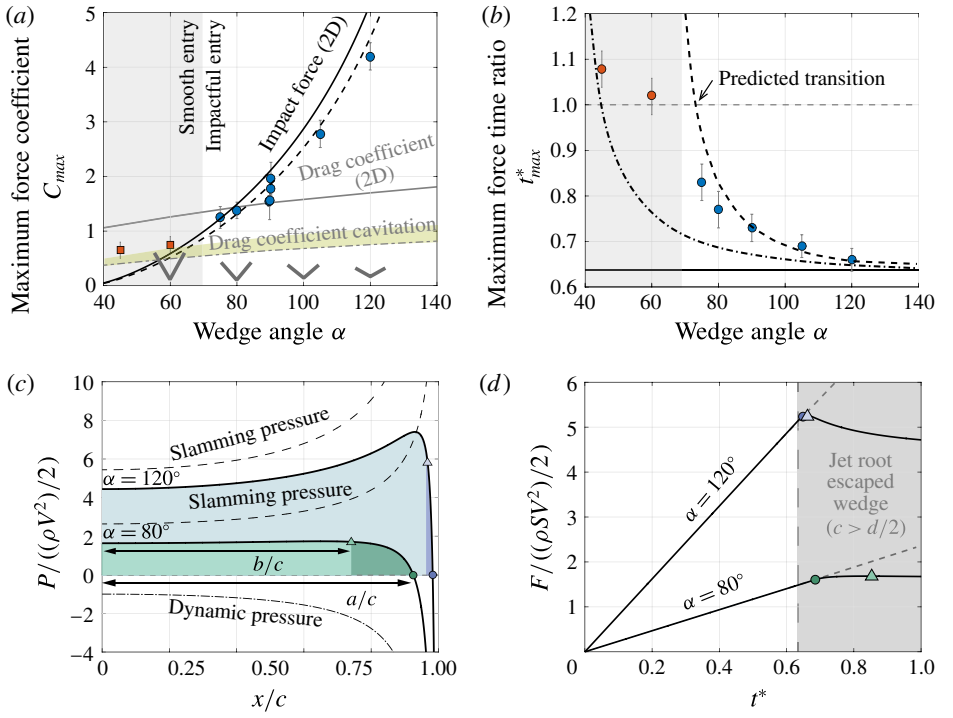


FIGURE 3. (Colour online) (*a*) The maximum force coefficient increases sharply with wedge angle α, and follows theoretical predictions by Logvinovich (1972) (solid line); excellent agreement is observed when Logvinovich's two-dimensional theory is corrected for finite aspect ratio $L/d = 4.2$ (dashed line). (*b*) For $\alpha \leqslant 70°$, the maximum force happens roughly when the wedge is fully submerged ($t^*_{max} \approx 1$), while for $\alpha > 70°$, t^*_{max} drops sharply and converges to the naive prediction from Wagner's theory $t^*_{max} = 2/\pi$. (*c*,*d*) The theoretical pressure profile can be used to improve the prediction for t^*_{max}. Assuming the maximum force occurs when the negative pressure area completely escapes the wedge ($a = d/2$, circles) leads to an analytical, refined estimation (dash-dotted line in panel *b*). In reality, the pressure integral (force F) on the wedge reaches a maximum when $b = d/2$ (triangles), leading to a second numerical prediction (dashed line in panel *b*), providing the same trend as the experimental measurements. Transition to smooth entry is expected when the peak force occurs after the wedge's submersion, that is, $t \geqslant 1$ (arrow in *b*). In (*a*,*b*), red square data points denote smooth entry, defined as the absence of prominent peak.

$t^* \leqslant 1$, confirming that the force and time scales are appropriate. From these graphs, we extract a single value of the maximum force C_{max}. We also mark the time t^*_{max} when the maximum force happens: $t^*_{max} = 0.66,\ 0.73,\ 1$ for $\alpha = 120°,\ 90°,\ 60°$, respectively. For $t^* > 1$, the force measurements do not collapse. We observe larger force coefficients at smaller entry velocities, particularly obvious for $\alpha = 120°$, which can be attributed to hydrostatic forces becoming significant as the Froude number approaches unity.

These measurements are repeated with wedge angles $\alpha = 60°,\ 75°,\ 80°,\ 90°,\ 105°$ and $120°$, leading to the values of C_{max} and t^*_{max} shown in figure 3(*a*,*b*) and table 1. Rather intuitively, C_{max} increases sharply with α, starting at $C_{max} = 0.65$ for $\alpha = 45°$ and reaching $C_{max} = 4.2$ for $\alpha = 120°$, while t^*_{max} decreases with α, starting at

https://doi.org/10.1017/jfm.2018.273 Published online by Cambridge University Press

α (deg.)	C_{max}	C_{max} (theory)	t^*_{max}	t^*_{max} (theory)
45	0.65 ± 0.3	0.15	1.08 ± 0.04	—
60	0.75 ± 0.3	0.58	1.02 ± 0.04	—
75	1.25 ± 0.3	1.24	0.83 ± 0.07	0.947
80	1.38 ± 0.3	1.75	0.77 ± 0.09	0.833
90	1.7 ± 0.3	2.08	0.73 ± 0.3	0.734
102	2.78 ± 0.3	3.25	0.69 ± 0.025	0.686
120	4.2 ± 0.3	5.15	0.66 ± 0.025	0.656

TABLE 1. Measured and theoretical force coefficient C_{max} and time ratio t^*_{max} (occurrence of maximum force).

$t^*_{max} = 1.08$ for $\alpha = 45°$ and plummeting to $t^*_{max} = 0.66$ for $\alpha = 120°$. No prominent peak force was observed for wedges with $\alpha \lesssim 70°$.

3.2. *Force model*

We show that (i) our experimental data compares favourably with Logvinovich's model once three-dimensional effects are taken into account and (ii) the transition between smooth and impactful entry, occurring at $\alpha \approx 70°$, can be anticipated using the same model.

Following Logvinovich (1972), we consider the diving of a two-dimensional wedge of opening angle α in the (x, z) plane, with the wedge crossing the interface at a constant velocity V. For convenience, we define the deadrise angle $\beta = (\pi - \alpha)/2$. The hydrodynamic pressure everywhere in the fluid domain is given by the unsteady Bernoulli equation,

$$p(x, z, t) = -\rho \left(\frac{\mathrm{d}\varphi}{\mathrm{d}t} + \frac{1}{2} |\nabla \varphi|^2 \right), \tag{3.1}$$

where φ is the velocity potential due to a horizontally expanding flat plate (plate of non-constant length to emulate the diving wedge) located on the free surface $z = 0$ (see, for example, Howison, Hockendon & Wilson 1991):

$$\varphi = -V \sqrt{c(t)^2 - x^2}. \tag{3.2}$$

Here, c is the location of the jet root defined as the extremity of the wetted surface (see figure 1*a*), and is given by the so-called 'Wagner condition':

$$c(t) = \pi V t / (2 \tan \beta). \tag{3.3}$$

Relation (3.2) is valid for $|x| < c(t)$, everywhere below the wedge's wetted surface. The prediction of $c(t)$ is well supported by experimental measurements, as we show in § 4.1. The pressure on the contact region is given by (Korobkin 2004)

$$P(x, t) = -\rho \left[\phi_t + \tfrac{1}{2} V \sin(2\beta) \phi_x + \tfrac{1}{2} \cos(\beta)^2 (\phi_x^2 - V^2) \right], \tag{3.4}$$

where ϕ is the velocity potential on the wedge's surface, related to φ via the approximation

$$\phi(x, t) \approx \varphi(x, 0, t) - V^2 t = -V \sqrt{c(t)^2 - x^2} + V^2 t. \tag{3.5}$$

https://doi.org/10.1017/jfm.2018.273 Published online by Cambridge University Press

For $\beta \ll 1$, (3.4) becomes

$$P(x,\,t) = -\rho\left[\phi_t + \tfrac{1}{2}(\phi_x^2 - V^2)\right]. \tag{3.6}$$

Substituting (3.5) into (3.6) leads to the approximate pressure distribution along the wedge:

$$P(x,\,t) = \frac{1}{2}\rho V^2\left[\frac{\pi}{\tan\beta}\frac{c}{\sqrt{c^2-x^2}} - \frac{c^2}{c^2-x^2}\right]. \tag{3.7}$$

The first term in (3.7), called the 'slamming pressure', comes from the unsteady pressure contribution in Bernoulli's equation and is associated with the rate of change of momentum of the added mass (Faltinsen 2005). The second term comes from the quadratic term and represents the dynamic pressure contribution. Figure 3(*c*) shows the non-dimensional pressure $P(x,\,t)/(\rho V^2)/2$ as a function of x/c, as well as the two contributions given by the first and second terms on the right-hand side of (3.7). The slamming pressure increases with distance from the wedge's keel and diverges at $x = c$; it also depends on the deadrise angle β of the wedge. In contrast, the dynamic pressure is maximum at the keel and decreases with x, tending to $-\infty$ as $x \to c$, and is independent of the wedge's angle. The total pressure is positive on most of the wetted region but becomes negative close to the jet root due to the dynamic pressure term. The sign change happens at $a/c = \sqrt{1-(\tan\beta/\pi)^2}$ (marked by circular symbols in figure 3*c*). This singularity is common to most modified Wagner models. It is regularized using the ansatz that only positive pressure matters (Logvinovich 1972; Korobkin 2004): pressure should be integrated from $x = 0$ to $x = a$, which yields (accounting for both sides of the wedge)

$$F(t) = 2\int_0^{a(t)} P(x,\,t)\,\mathrm{d}x = \rho V^2 c(t)\left[\frac{\pi^2}{2\tan\beta} - K(\beta)\right], \tag{3.8}$$

where

$$K(\beta) = \frac{\pi}{\tan\beta}\left[\frac{\pi}{2} - \arcsin\,(a/c)\right] - \frac{1}{2}\ln\left[\frac{1+a/c}{1-a/c}\right]. \tag{3.9}$$

To predict the maximum force, we assume that it is reached when the wetted length c equals the wedge's half-width $d/2$, that is to say, when the splash root escapes the wedge. From (3.3), we get that $t^*_{max} = 2/\pi \approx 0.636$, independently of α. Substituting this prediction for t^*_{max} into (3.8), (3.9) leads to

$$F_{max} = \frac{1}{2}\rho S V^2\left[\frac{\pi^2}{2\tan\beta} - K(\beta)\right]. \tag{3.10}$$

In figure 3(*a*,*b*), we compare $F_{max}/(\rho S V^2)/2$ and t^*_{max} (solid lines) to experimental data. The prediction for t^*_{max} matches roughly with the experimental data for large α, but the discrepancy increases sharply as α decreases. The force prediction $F_{max}/(\rho S V^2)/2$ is consistently larger (by approximately 15 %) than the force data for $\alpha > 90°$. One reason for this discrepancy stems from the fact that the prediction is based on two-dimensional theory while our wedges are not infinitely long ($L/d = 4.2$); it is thus necessary to consider three-dimensional effects. Following the suggestion of Zhao *et al.* (1996), we correct Logvinovich's two-dimensional prediction using results of Meyerhoff (1970), who calculated the added mass coefficients of rectangular plates of various length-to-width ratio. His calculations show that in order to accurately

https://doi.org/10.1017/jfm.2018.273 Published online by Cambridge University Press

represent the effect of finite aspect ratio in situations where added mass plays an important role, two-dimensional predictions have to be corrected by a factor approximately equal to $1 - d/(2L)$. This results in a 12 % decrease in maximum force (dashed line in figure 3*a*), which is in good agreement with the experimental data for moderate and large wedge angles.

The values of F_{max} and t_{max} are based on the assumption that the maximum force happens when $c = d/2$. Yet, the theoretical pressure profile along the wetted length (figure 3*c*) is negative from $x = a$ to $x = c$. To refine the prediction of t_{max}, we consider the maximum force to happen when the region of negative pressure has completely escaped the wedge (that is, when $a = d/2$), which yields $t^*_{max} = (2/\pi)(c/a) = (2/\pi)/\sqrt{1 - (2\tan\beta/\pi)^2}$. This improved prediction, represented in figure 3(*b*) as a dash-dotted line, increases sharply as α decreases, but underestimates the experimental results, especially for moderate to large wedge angles. To refine the prediction further, we note that the integral of the pressure profile on the wedge continues to increase until $b = d/2$, as shown in figure 3(*c*,*d*) (triangles). Numerical computation of this integral leads to a refined estimate of t^*_{max}, represented as a dashed line in figure 3(*b*). This estimate is now in reasonable agreement with the experimental values for wedge angles down to $\alpha \approx 80°$.

We now use the model to predict the transition from smooth and impactful entry. To this end, recall that the pressure on the wedge consists of two components: the 'slamming' pressure, which sharply increases with α, and the dynamic pressure, which is independent of α. For $\alpha = 120°$, the slamming pressure dominates, inducing a prominent peak in the pressure profile in figure 3(*c*). Consequently, the maximum force (indicated by triangles in figure 3*c*) occurs immediately after the jet root leaves the wedge at $t^*_{max} \approx 2/\pi \simeq 0.636$. This peak force before wedge submersion is characteristic of the impactful regime (see figure 2). As the wedge becomes sharper, the relative importance of the dynamic pressure increases and the pressure profile becomes flatter (figure 3*c*). As a result, the time to reach the maximum force progressively increases. As it passes $t^*_{max} = 1$ (wedge fully submerged), the entry is expected to be smooth: no peak before wedge submersion. This transition criterion gives $\alpha \simeq 73°$ (arrow in figure 3*b*), in good agreement with the observed transition, between 60° and 75°. The important conclusion here is that the transition between the smooth and impactful regimes is expected to happen when the unsteady 'slamming' pressure has an effect comparable to the dynamic pressure, that is to say, when the rate of change of added mass is no longer the dominant effect. See supplementary movie 1, available at https://doi.org/10.1017/jfm.2018.273, for an illustration of the entry force in the smooth and impactful regimes.

Finally, it is interesting to compare the peak force with the drag force of a completely submerged wedge (figure 3*a*). For large wedge angles, the peak force is significantly higher than the drag force. However, the peak force decreases sharply with the opening angle and, for $\alpha < 80°$, the measured maximum force becomes comparable to the drag coefficient of an immersed wedge. As α decreases further, the peak force continues to decrease, in agreement with the impact force theory, to approximately half of the submerged drag force. This low value reflects that the drag force acting on diving wedges is smaller than we would expect for an immersed wedge, as we will explain in greater detail in the next section.

3.3. *Drag force with a cavity*

After submersion, the wedge reaches a quasi-steady regime characterized by a relatively small vertical force (figure 4). The measured force (dash-dotted line in figure 4) is significantly lower than the drag force on an immersed wedge of the

https://doi.org/10.1017/jfm.2018.273 Published online by Cambridge University Press

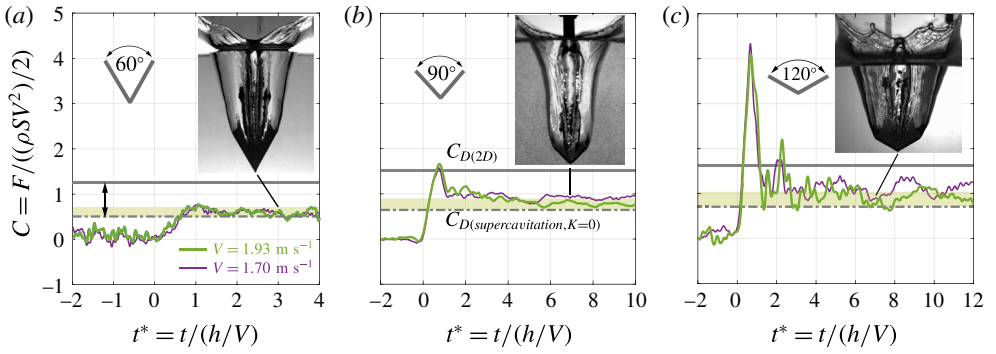


FIGURE 4. (Colour online) Force history on wedges with opening angles $\alpha = 60°, 90°, 120°$, in the limit of small hydrostatic effects ($Fr > 2.8$). The non-dimensional drag force on the entering wedge is significantly smaller than the corresponding drag coefficients of an immersed wedge (solid grey line); it matches the drag force measured on cavitating wedges (dash-dotted line and green overlay).

same angle. The obvious difference between the two cases is the presence of the cavity in the wake of the diving wedge; see figure 5. The cavity has a notable effect on the wake of the wedge. There is no systematic model of how transient cavities affect drag on translating bodies; however, the influence of cavities on drag has been studied extensively in the context of cavitation (Knapp *et al.* 1970). Cavitation studies show that the presence of the cavity induces a dramatic reduction in drag, in the range two to three times. The reduction depends on the cavitation number $K = (p_\infty - p_{vap})/(\rho V^2)/2$, which compares the drop in Bernoulli pressure $(\rho V^2)/2$ with the pressure drop needed to reach vapour pressure $p_\infty - p_{vap}$ in order for cavitation to happen. Here, p_∞ is the pressure far away from the object. Typically, complete cavitation is reported for values up to $K \approx 0.4$, and partial cavitation happens beyond this value (Knapp *et al.* 1970). Because the cavities in the present work are fully formed, a sensible range of value for K is between 0 and 0.4. According to Knapp *et al.* (1970) steady drag coefficients for supercavitating wedges can be expressed as $C_D = C_{D_o}(1 + K)$, with C_{D_o} ranging from 0.489 to 0.745 for $\alpha = 60°$ and $\alpha = 120°$. The corresponding ranges of C_D, with K varying from 0 to 0.4, are reported as a light khaki zone in figure 4 for each wedge angle. The experimental force measurements exhibit residual oscillations due to the drop mechanism. Oscillations notwithstanding, the predictions proved to be in good agreement with experimental data. It indicates that transient (inertial) cavities affect drag in the same way as cavitation.

4. Splash model

Snapshots of the splash and cavity shapes of a 90° wedge entering water are shown at two time instants $t^* = 2$ and $t^* = 4$ in figure 6. At $t^* = 2$, the cavity and splash corresponding to different entry velocities V have the same form (figure 6*a*) but at $t^* = 4$ the splashes exhibit notable differences (figure 6*b*); at larger entry velocities, splashes extend further and develop a characteristic doubly curved shape that we call 'arabesque'. The fact that the splashes coincide well at short times but not at longer times suggests that these variations are not due to initial conditions. To investigate the physics of the splash evolution, we develop a one-dimensional model of the splash using first principles and empirical observations.

https://doi.org/10.1017/jfm.2018.273 Published online by Cambridge University Press

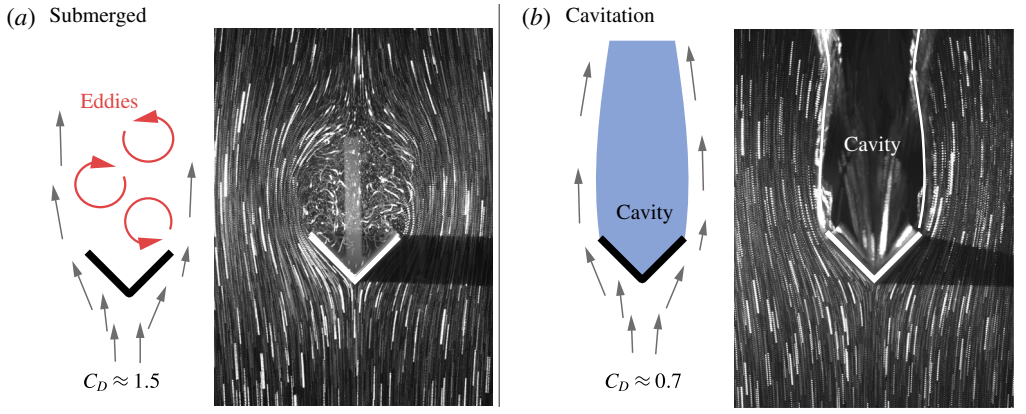


FIGURE 5. (Colour online) Cavity and drag reduction. The presence of a transient cavity induces striking changes in the wedge's wake and dramatically reduces the drag on the wedge. $\alpha = 90°$, $V \simeq 1$ m s^{-1}. Equivalent exposure for both pictures is $\Delta t = 12$ ms.

4.1. *Splash ejection: empirical observations*

Using high-speed video recordings (see figure 7*a* for an example), we systematically measure three relevant parameters of the splash kinematics at short times: the wetted length c, jet speed V_{so} and jet angle θ_o.

Raw measurements of V_{so} as a function of entry velocity V are shown in figure 7(*b*). Clearly, V_{so} is linearly proportional to V, even at low entry speeds, and the coefficient of proportionality V_{so}/V is an increasing function of α. In figure 7(*c*), we plot V_{so}/V versus α and compare it to the expansion speed of the wetted length $\dot{c}/V$ obtained experimentally (purple squares) and theoretically (solid line) based on equation (3.3):

$$\frac{V_{so}}{V} = 1.55\left(\frac{\dot{c}}{V}\right) = \frac{1.55\pi}{2\tan\beta}. \tag{4.1}$$

The jet angle θ_o between the trajectory of the water particles in the jet and the horizontal axis is reported in figure 7(*d*). The schematic in figure 7(*e*) highlights the theoretical predictions of θ_o and V_{so}/V assuming that the jet stays in contact with the wedge's surface, leading to the implicit equation for θ_o,

$$\frac{\tan\alpha}{\cos\theta_o - \sin\theta_o\tan\alpha} = \frac{V_{so}}{V}. \tag{4.2}$$

Figure 7(*d*) shows that the theoretical predictions are in good agreement with the experimental measurements. Taken together, these observations imply that Wagner's approach allows us to predict both the initial jet tip velocity V_{so} and jet ejection angle θ_o, given a single corrective parameter (the 1.55 constant) that is independent of α. We are now equipped to tackle the long-term evolution of the splash shape past the initial submersion of the wedge.

4.2. *Splash model: kinematics and initial conditions*

We develop a discrete fluid particle model of the splash based on the idea that the splash is primarily ballistic. The splash is represented by a succession of discrete

https://doi.org/10.1017/jfm.2018.273 Published online by Cambridge University Press

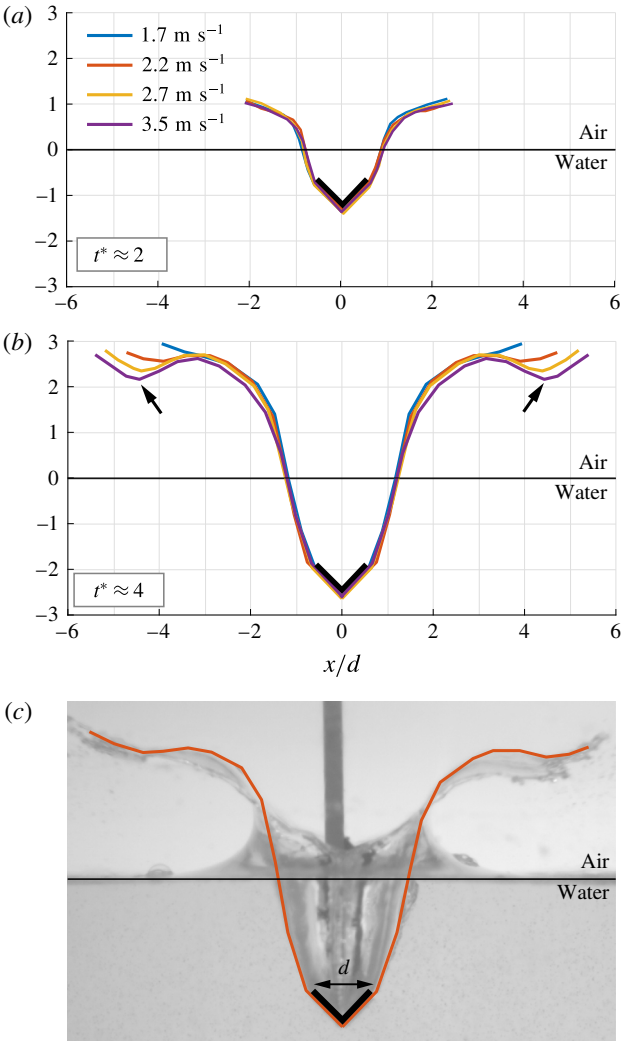


FIGURE 6. (Colour online) Shape reconstruction for $\alpha = 90°$, at $t^* \approx 2$ (*a*) and $t^* \approx 4$ (*b*), in the limit of vanishing gravity effects ($V = 1.7$–2.5 m s^{-1}, $Fr = 4$–8). (*c*) Example of reconstruction for $V = 2.2$ m s^{-1} ($Fr = 5.2$), at $t^* \approx 4$. The cavity is self-similar at all times, but the splash develops noticeable differences: as the entry velocity increases, the splash extends further and develops a double curvature. Notice the swelling of the dip (arrows).

particles P_j, $j = 1, 2, 3, \ldots \in \mathbb{N}$. Particle j is located at $\boldsymbol{r}_j = x(P_j, t)\boldsymbol{e}_1 + z(P_j, t)\boldsymbol{e}_3$, where P_j is a Lagrangian label of particle j, and moves at a velocity $\boldsymbol{v}_j = v_x(P_j, t)\boldsymbol{e}_1 + v_z(P_j, t)\boldsymbol{e}_3$ under the influence of gravity, surface tension, and aerodynamic forces.

Particles are initially ejected from the water surface ($z = 0$) at a shooting point $x(P_j, t_j)$, where t_j represents the time of ejection of particle j. Our goal in this section is to determine the initial conditions, shooting position and velocity, for each particle. To this end, it is convenient to represent the velocity $\boldsymbol{v}_j$ of particle j by its speed $V_s(P_j, t)$ and pitch angle $\theta(P_j, t)$ measured from the horizontal.

https://doi.org/10.1017/jfm.2018.273 Published online by Cambridge University Press

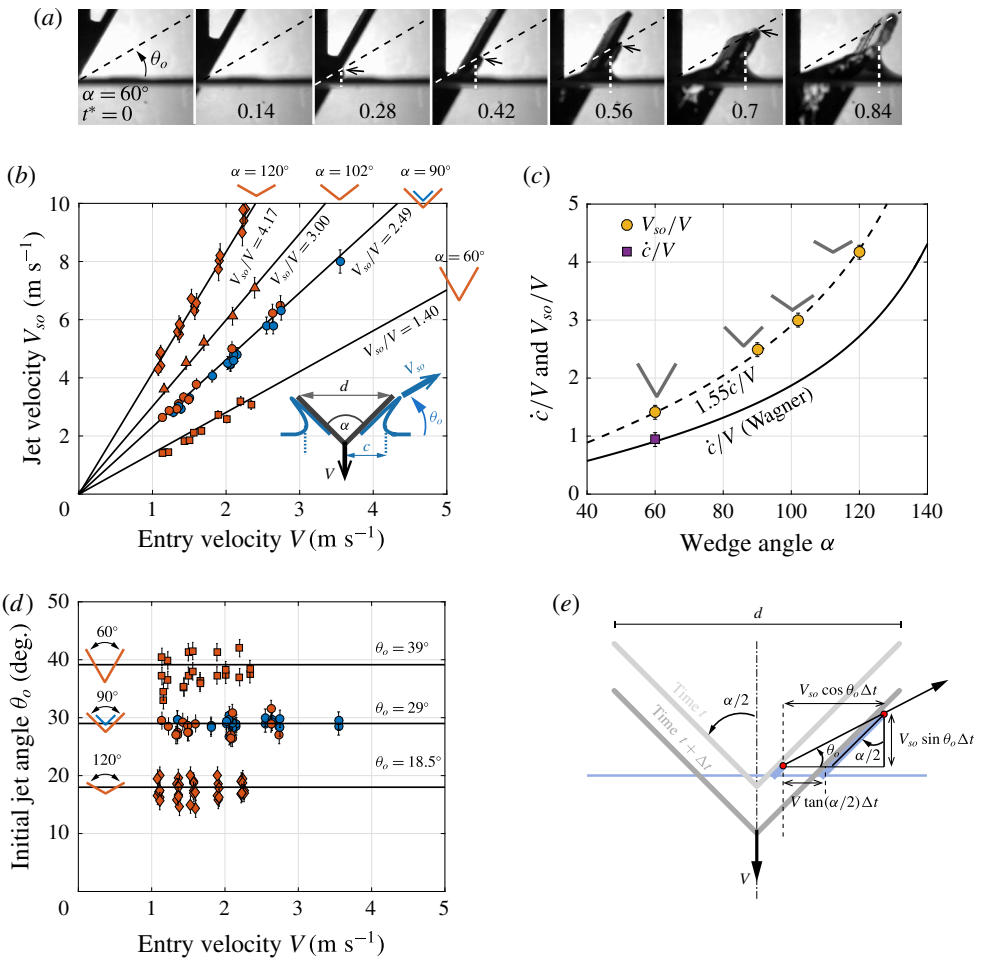


FIGURE 7. (Colour online) Jet root expansion and jet velocity, measured from high-speed video (*a*); the vertical white dashed line shows the location of the jet root; the black arrow shows the jet tip. (*b*) Splash tip velocity V_{so} is proportional to entry velocity V. (*c*) The coefficient of proportionality increases with α, and is measured to be $1.55 \times \dot{c}/V$. (*d*) The initial jet angle is independent of V. (*e*) Before submersion, the shooting velocity and pitch angle are constant in time, as imposed by the non-penetration condition.

Before the wedge is fully submerged, we make the assumption that the shooting point is located at the intersection of the undisturbed water surface with the wedge given by $x = Vt_j \tan(\alpha)$, and all particles are assumed to eject with the same velocity V_{so} and angle θ_o (figure 8*a*). That is to say, for ejection time $t_j \leqslant h/V$, the initial conditions of particle P_j are given by

$$V_s(P_j, t_j) = V_{so}, \quad \theta(P_j, t_j) = \theta_o, \quad x(P_j, t_j) = Vt_j \tan(\alpha). \tag{4.3a–c}$$

This assumption is in agreement with the actual interface shape below the wedge (see figure 7) in that we consider the fluid pile-up as part of the splash.

After submersion, $t_j \geqslant h/V$, the shooting point is located at the cavity wall $w(z = 0) = w_o$, where w is the cavity half-width and w_o is the value of w at the free water

https://doi.org/10.1017/jfm.2018.273 Published online by Cambridge University Press

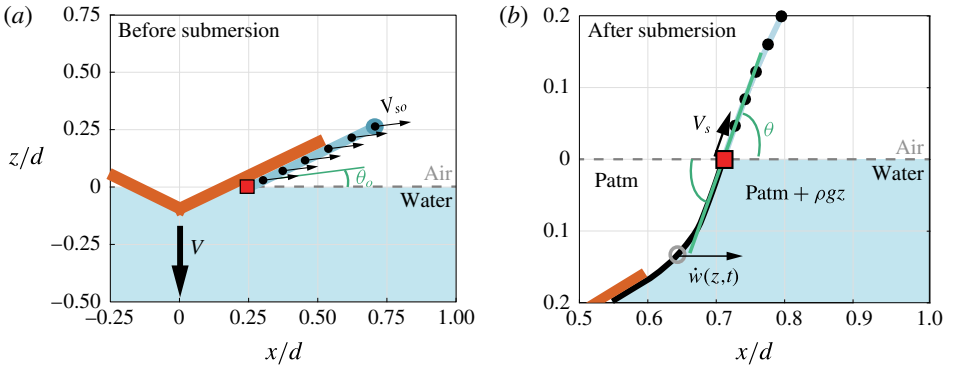


FIGURE 8. (Colour online) Initial conditions applied to shooting particles. (*a*) For times before wedge submersion, particles are shot with constant velocity V_{so} and angle $\theta = \theta_0$. (*b*) After submersion, θ is adjusted to maintain continuity with the cavity shape, and the shooting velocity V_s decreases exponentially.

surface ($z = 0$); see figure 8(*b*). The initial shooting conditions are now dependent on the time of ejection t_j. Namely, the shooting velocity decreases with time and eventually decays to 0 while the base of the splash becomes steeper with time. We consider the ejection velocity to decrease exponentially such that

$$V_s(P_j, t_j) = V_{so} \mathrm{e}^{-(t_j - h/V)/\tau_s}, \tag{4.4}$$

where τ_s is a parameter that we set to $\tau_s = 0.025/V$ regardless of the wedge angle.

An implicit expression for the initial ejection angle $\theta(P_j, t_j)$ can be obtained by considering continuity between the slope of the splash and the slope of the cavity $w'_o = \mathrm{d}w/\mathrm{d}z|_{z=0}$,

$$\frac{V_s(P_j, t_j)\sin(\theta(P_j, t_j))}{V_s(P_j, t_j)\cos(\theta(P_j, t_j)) - \dot{w}_o(t_j)} = \tan(w'_o(t_j)). \tag{4.5}$$

Here, $\dot{w}_o(t_j)$ and $w'_o(t_j)$ are, respectively, the horizontal speed and the slope of the cavity at $z = 0$ and $t = t_j$.

To close the system in (4.4) and (4.5), we need a model for the time evolution of the cavity wall w. Duclaux *et al.* (2007) applied a slice-averaged model to the transient dynamics of axisymmetric cavities created by spherical or cylindrical bodies. Using an unsteady potential flow model per slice, Duclaux *et al.* (2007) found that the evolution of the cavity radius R can be described at each value of z by the Rayleigh–Plesset equation, $R\ddot{R} + (3/2)\dot{R}^2 = \Delta p$, where $\Delta p = -gz$ is the pressure difference between the inside and the outside of the cavity at depth z, assuming atmospheric pressure inside the cavity. This equation is not directly applicable to wedges – one would have to derive a new analytic expression for the slice-averaged flow potential assuming the wedge is infinitely long. However, because our wedges have a relatively short aspect ratio L/d, we make the assumption that the equation derived in Duclaux *et al.* (2007) applies in a modified form. Namely, we postulate that

$$w\ddot{w} + \tfrac{3}{2}C_c\dot{w}^2 = -gz, \tag{4.6}$$

where C_c is an *ad hoc* parameter (equal to 1 for axisymmetric cavities). By definition, C_c is independent of V, but we expect it to depend on the geometry of the wedge,

https://doi.org/10.1017/jfm.2018.273 Published online by Cambridge University Press

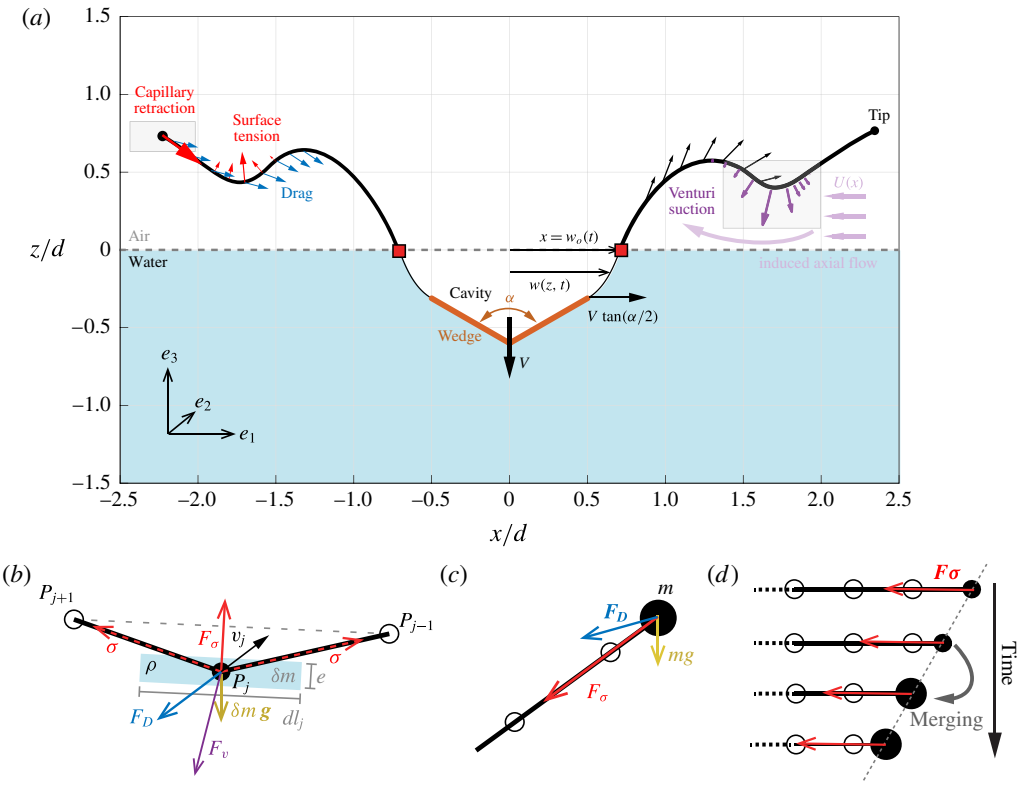


FIGURE 9. (Colour online) (*a*) Overview of the model and physical processes. The pitch angle is tied to the cavity local slope, and the shooting velocity decreases exponentially in time. Particles are subject to weight, drag, surface tension, and Venturi-induced suction. (*b–d*) Schematic representation of forces on an individual particle: (*b*) anywhere along the splash, and (*c*) at the tip, where capillary retraction takes place. (*d*) Initial stages of capillary retraction, showing the first particle merging. A straightforward merging routine allows the retraction speed to quickly converges to the Taylor–Culick velocity $V_\sigma = \sqrt{2\sigma/\rho e}$, independently of the merging threshold.

represented by the aspect ratio L/d and opening angle α. The value of C_c is adjusted for each wedge, by matching the cavity dynamics to high-speed experimental images. To obtain the cavity dynamics, we solve (4.6) per slice for all slices from the top of the submerged wedge to the undisturbed water surface subject to initial conditions $w(t=0) = d/2$ and $\dot{w}(t=0) = V \tan\alpha$.

Put together, equations (4.4), (4.5) and (4.6) form a closed set of equations that determine the initial conditions $V_s(P_j, t_j)$, $\theta(P_j, t_j)$ and $x(P_j, t_j)$ for the ejection of particle P_j for $t_j \geqslant h/V$.

4.3. *Splash model: force balance*

Figure 9(*a*) shows an overview of the physical processes affecting the splash and the cavity evolution during water entry. Particles are shot at regular intervals of time in such a way to be initially separated by a constant distance $d\ell_o$. The mass per unit length attributed to each particle is $\delta m = \rho e_o d\ell_o$, where e_o is the initial thickness of the splash sheet, assumed to be constant during splash ejection. Each particle is subject

https://doi.org/10.1017/jfm.2018.273 Published online by Cambridge University Press

to the following forces: weight $\delta m\boldsymbol{g}$, drag $\boldsymbol{F_D}$, surface tension $\boldsymbol{F_\sigma}$, and a Venturi-induced suction $\boldsymbol{F_V}$. All forces are expressed per unit length of the splash sheet unless otherwise stated. The force balance on particle j is given by

$$\delta m\frac{\mathrm{d}\boldsymbol{v}_j}{\mathrm{d}t} = \delta m\boldsymbol{g} + \boldsymbol{F_D} + \boldsymbol{F_\sigma} + \boldsymbol{F_V}. \tag{4.7}$$

Drag $\boldsymbol{F_D}$ on particle j is calculated by considering the splash segment $\Delta\boldsymbol{r}_j = \boldsymbol{r}_{j-1} - \boldsymbol{r}_{j+1}$ of length $d\ell_j = \|\Delta\boldsymbol{r}_j\|$, moving with velocity $\boldsymbol{v}_j$ at an angle of attack ψ_j defined as the angle between $\boldsymbol{v}_j$ and $\Delta\boldsymbol{r}_j$. This leads to (Andersen, Pesavento & Wang 2005)

$$\boldsymbol{F_D} = -\tfrac{1}{2}C_D\sin^2(\psi_j)\rho_a d\ell_j\|\boldsymbol{v}_j\|\boldsymbol{v}_j. \tag{4.8}$$

Here, C_D designates the drag coefficient for when the element is perpendicular to the incoming flow, which we fix at $C_D = 2.5$ for all experiments. The drag force is calculated using the absolute travelling velocity of the fluid particle, and not its velocity relative to the ambient air. The effect of the air flow is considered independently in the Venturi-suction force made explicit later on in this section.

Surface tension is accounted for in the most straightforward way: each particle experiences a longitudinal traction of magnitude σ from its closest neighbours, as represented in figure 9(*b*). For $j \neq 1$, one has

$$\boldsymbol{F_\sigma} = \sigma\left(\frac{\boldsymbol{r}_{j-1} - \boldsymbol{r}_j}{\|\boldsymbol{r}_{j-1} - \boldsymbol{r}_j\|} + \frac{\boldsymbol{r}_j - \boldsymbol{r}_{j+1}}{\|\boldsymbol{r}_j - \boldsymbol{r}_{j+1}\|}\right). \tag{4.9}$$

This force is normal to the local tangent $\Delta\boldsymbol{r}_j$, and acts as a restoring force: it tends to cancel any shape curvature. The particle at the tip ($j = 1$) is a particular case: surface tension results in only one longitudinal force directed towards its next neighbour, leading to the retraction of the particle at the tip (figure 9*c*). This retraction is observed in systems such as free sheets and ligaments (Marmottant & Villermaux 2004; Lhuissier & Villermaux 2009). The speed of retraction, relative to the sheet, is constant and known as the Taylor–Culick velocity $V_\sigma = \sqrt{2\sigma/\rho e}$ (Taylor 1959; Culick 1960). To account for capillary retraction in our model, the receding particle of initial mass δm has to merge with its successive closer neighbours, as shown in figure 9(*d*). When merging happens, (i) the new particle's mass increases by δm, (ii) the new particle is positioned at the centre of mass of the two former particles, and (iii) the new particle's momentum is the sum of the momentum of the two former ones. Given these conditions, we observe that the retraction speed of the tip particle quickly converged to V_σ, independently of the merging criteria (interparticle distance).

The Venturi-induced suction force $\boldsymbol{F_V}$ has a significant effect on the late-stage development of the sheet. This suction happens because the motion of the splash dome induces an axial flow of air rushing in to fill the expanding chamber beneath it, as represented in figure 10. The air is accelerated through the gap between the undisturbed water surface and the lower part of the splash, causing the pressure to drop and generating a downward suction. To calculate this suction force, we begin by evaluating the volume $\Omega(x, t)$ of the chamber under the splash

$$\Omega(x, t) = \int_{x_o}^{x} Z(\tilde{x}, t)\,\mathrm{d}\tilde{x}, \tag{4.10}$$

https://doi.org/10.1017/jfm.2018.273 Published online by Cambridge University Press

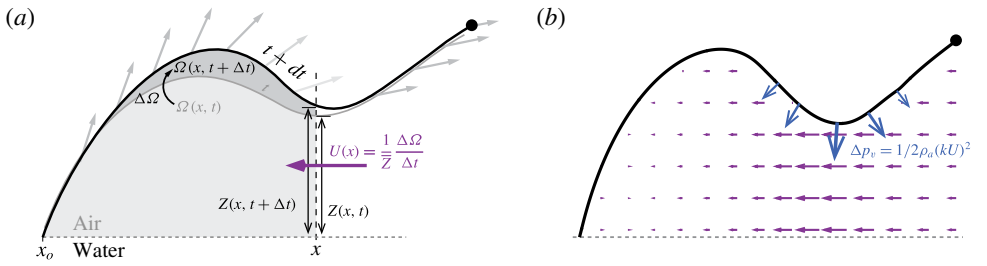


FIGURE 10. (Colour online) (*a*) Average axial velocity into the chamber is determined using volume conservation. (*b*) Typical calculated axial flow field (purple) and resulting suction force on the sheet (blue).

where x_o is the position of the base of the splash and $Z(x,t)$ refers to the local height of the splash above the free water surface. Assuming the chamber is two-dimensional – that is, no flow in the direction perpendicular to the drawing plane – the average volume change $\Delta\Omega(x,t)=\Omega(x,t+\Delta t)-\Omega(x,t)$ of the splash is related to the average flow $U(x,t)$ passing through the section $\bar{Z}=([Z(x,t)+Z(x,t+\Delta t)])/2$, yielding

$$U=\frac{1}{\bar{Z}}\frac{\Delta\Omega}{\Delta t}. \tag{4.11}$$

Using Bernoulli's principle between a position far away from the splash and the bottom of the sheet, we can estimate the pressure drop as $\Delta p_v=-(\rho_a(kU)^2)/2$, where kU is the corrected axial velocity. The correction factor k accounts for the difference between the real system and the idealized model, including non-uniformity of this velocity in the vertical direction and three-dimensional effects. We expect k to depend on α: k converges to 1 as α approaches 180° because the splash evolves closer to the water surface and the lubrication approximation becomes more justified. We set $k=1.5$ for all computations presented in § 5 ($\alpha=120°$). The magnitude of the suction force $\boldsymbol{F_V}$ at particle P_j is given by $\Delta p_v d\ell_j$, where Δp_v is evaluated at $x=x(P_j,t)$ and $d\ell_j=\|\Delta\boldsymbol{r}_j\|$, as previously defined. The direction of $\boldsymbol{F_V}$ is along the local normal $\Delta\boldsymbol{r}_j^{\perp}/\|\Delta\boldsymbol{r}_j\|$ to the sheet, namely,

$$\boldsymbol{F_V}=-\tfrac{1}{2}\rho_a(kU)^2\Delta\boldsymbol{r}_j^{\perp}. \tag{4.12}$$

We substitute expressions (4.8), (4.9) and (4.12) for $\boldsymbol{F_D}$, $\boldsymbol{F_\sigma}$ and $\boldsymbol{F_V}$ into (4.7). The resulting equations are integrated using an explicit forward Euler method with typical time step $dt=10^{-6}$ s. The initial distance between particles $d\ell_o=100$ μm is chosen to be of the order of the sheet thickness.

5. Splash evolution

Figure 11 presents the evolution of the splash following the impact of a 120° wedge of width $d=36$ mm on the water surface at $V=1.92$ m s^{-1}. The ejecta deforms into a fairly complex shape, characterized by two inversions of curvature from its base to its rim. Of particular interest is the formation of a dip, resulting from the strong downward pull of the thinnest and lowest part of the splash. As we demonstrate in the following, the existence of this singular feature is tied to two key ingredients: the generation of a kink at short times and the growth of this kink, favoured by aerodynamics and hindered by surface tension (figure 11*b–d*). We also show that for

https://doi.org/10.1017/jfm.2018.273 Published online by Cambridge University Press

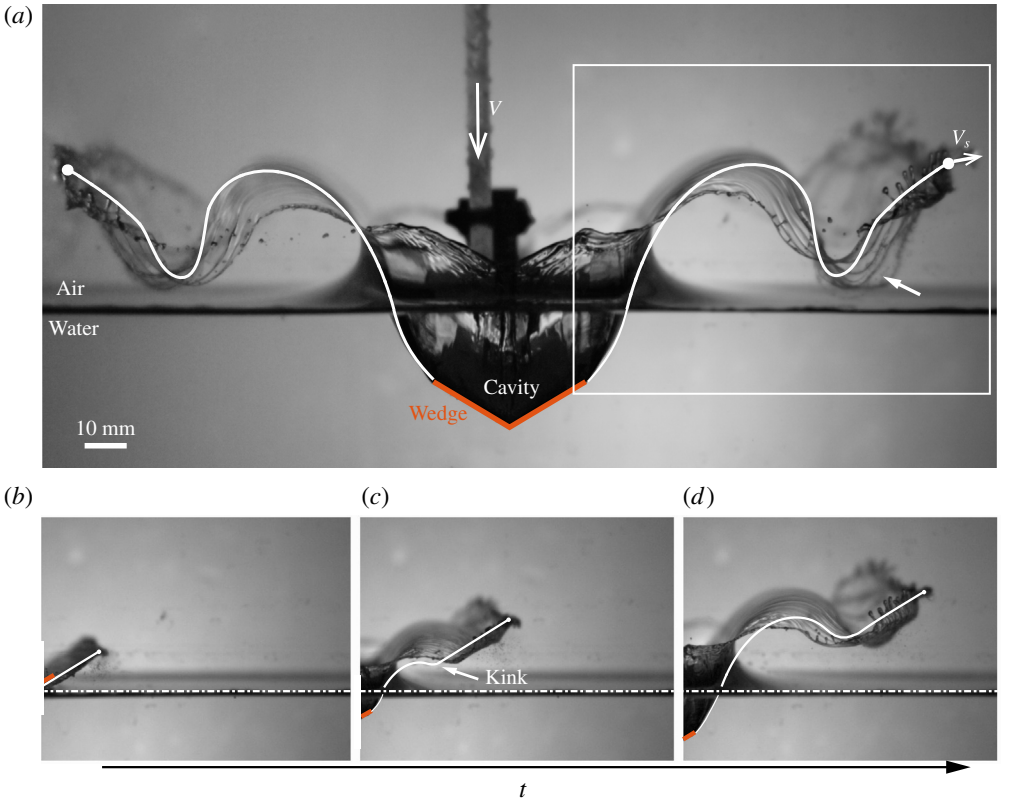


FIGURE 11. (Colour online) (*a*) Snapshot taken 15 ms after impact of a $\alpha = 120°$ wedge in water at $V = 1.92$ m s^{-1}, and (*b–d*) preceding time evolution of the splash sheet; snapshots are 3.1 ms apart. The leading part of the sheet is ejected with a speed $V_s \approx 4.5$ m s^{-1}. Note the strong downward suction of part of the splash sheet (white arrows) leading to its rapid fragmentation (see also supplementary movie 2). Computed shapes are superimposed in white.

moderate and large wedge angles, the Venturi effect is the dominant aerodynamic force driving the splash deformation.

To highlight the effect of entry velocity, we reproduce in figure 12(*a–c*) three snapshots for gradually increasing entry velocity $V = 1.11$, 1.53 and 1.92 m s^{-1}, taken at the same dimensionless time $t^* = 2.8$. The snapshots are similar in many ways. Looking below the free water surface, the wedge's penetration and cavity shapes are virtually the same. Above the free surface, the splash shapes share some similarities. For instance, the sheet rim, at the far right of each picture, is nearly at the same location. There is, however, one major difference between the three snapshots: the depth of the depression. In figure 12(*a*), the lowest part of the dip is at approximately half the height of the dome, while in figure 12(*c*), the depression nearly reaches the water surface. This difference can be, erroneously, attributed to the effect of drag on the fast-moving sheet. We shall show that this idea is essentially wrong, and while drag does have a significant effect on the water sheet, it only contributes little to the strong downward pull the dip of the splash sheet is subject to. Figure 12(*d–g*) uses our model to quantify the effect of various forces on the splash shape. Drag and surface tension, alone or combined, generate splash shapes that are nearly identical

https://doi.org/10.1017/jfm.2018.273 Published online by Cambridge University Press

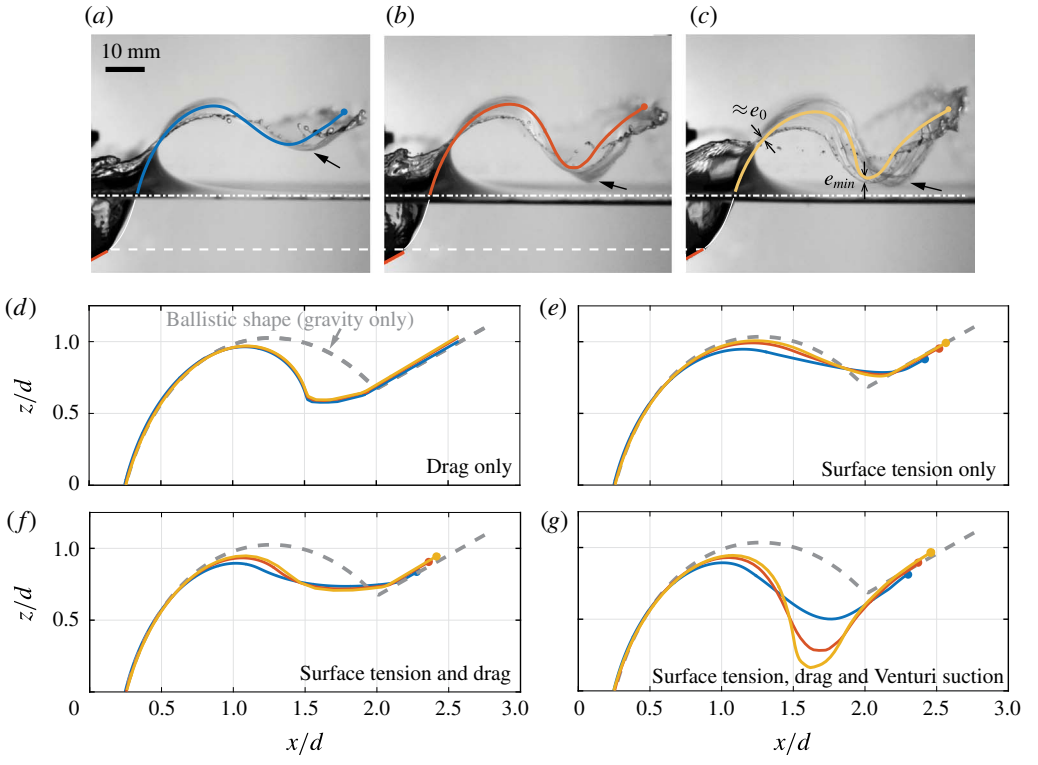


FIGURE 12. (Colour online) (*a–c*) Experimental snapshots and corresponding computed shapes taken at $t^* = t/(h/V) \approx 2.8$ after impact for increasing impact velocity V: 1.11, 1.53, 1.92 m s^{-1}. Note that the dip in the splash sheet (black arrow) gradually swells as velocity increases. Panel (*c*) shows the last computable shape at $t^* \approx 2.6$, for which the thinning ratio is $e_{min}/e_o \approx 1/30$. (*d–g*) Quantification of the effect of the various forces. While neither drag or surface tension can account for the bending, Venturi-mediated suction does.

at different entry velocities (labelled by colour in figure 12). Venturi suction is needed to be able to reproduce correctly the observed shapes and variation with V: the splash shape resulting from incorporating all forces is superimposed onto figure 12(*a*), showing excellent agreement between the one-dimensional model and the experimental observations.

5.1. *Splash depression*

In order to elucidate the nature of the vertical force causing the depression in the splash sheet, we examine the dynamics of the dip. In figure 13(*a*,*b*), we measure the vertical acceleration γ of a marker located at the local minima in the dip, designated by a red dot. The measurements are taken shortly after the downward dip becomes clear, in the time interval between the first two snapshots of figure 13. We find that acceleration is an increasing function of the splash velocity V_s and, consequently, of V, with values well above the gravitational acceleration: approximately $10g$ for the slowest velocity and up to $90g$ for $V_s = 2.35$ m s^{-1}. Importantly, we find that for $V_s > 7$, γ is proportional to V_s^2, suggesting the downward force has an aerodynamic origin.

https://doi.org/10.1017/jfm.2018.273 Published online by Cambridge University Press

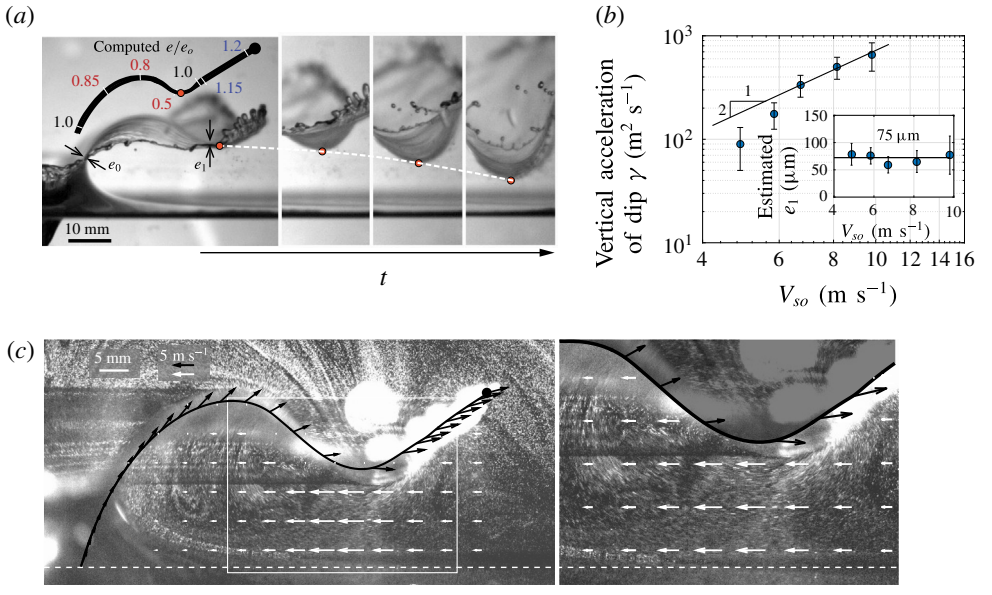


FIGURE 13. (Colour online) (*a*,*b*) Quantification of the strong downward pull on the thinnest ($e/e_o \approx 0.5$) part of splash sheet. When surface tension effects are negligible, the acceleration is proportional to V_{so}^2, suggesting a purely aerodynamic force. Assuming the associated aerodynamic pressure scales as $(\rho_a V_s^2)/2$ leads to an indirect estimate of the sheet thickness e_o. (*c*) Visualization of the fluid motion around the splash at $t^* = 0.7$ for $V = 1.36$ m s^{-1} using oil droplets, highlighting the axial flow into the expanding chamber beneath the splash sheet (see also supplementary movie 2). The estimated average axial velocity (white) from mass conservation show good qualitative agreement with the experiment. The splash sheet and the velocity of individual particles within the sheet as shown in black.

We push the analysis further in order to determine the local thickness e_1 (and, thus, the initial thickness e_o) and to derive a criterion for the growth of the dip. To this end, we write the force balance in the vertical direction on a small fluid element of length $d\ell$, width L and thickness e_1. The forces are drag $\boldsymbol{F}_D$, surface tension $\boldsymbol{F}_\sigma$ acting upwards, and an aerodynamically related downward suction $\boldsymbol{F}_V = (\rho_a d\ell L V_s^2)/2$. We ignore $\boldsymbol{F}_D$ because the vertical velocity of the marker is at least five times smaller than V_s. We are left with the force balance in the vertical direction $\rho e_1 L d\ell \gamma = \boldsymbol{F}_\sigma - \boldsymbol{F}_V$. Dividing throughout by $Ld\ell$, we get the balance law in terms of the pressure difference between a capillary contribution Δp_σ and an aerodynamic contribution $\Delta p_V = (\rho_a V_s^2)/2$,

$$\rho e_1 \gamma = -\Delta p_\sigma + \Delta p_V. \tag{5.1}$$

From (5.1), we expect the growth of the dip to be inhibited when the restoring effect of surface tension overcomes the destabilizing effect of the suction pressure.

To derive a criterion for predicting the dip growth, we assume that the local radius of curvature of the splash scales as the wedge's lateral size d, in qualitative agreement with observation. The capillary pressure contribution is thus $\Delta p_\sigma \approx 2\sigma/d$ across the two interfaces. Substituting into (5.1), we get the following criteria for the growth of the dip: $(\rho_a V_{so}^2 > 2\sigma/d)/2$. For $d = 36$ mm and $\rho_a = 1.25$ Kg m^{-3}, the criteria yield

https://doi.org/10.1017/jfm.2018.273 Published online by Cambridge University Press

$V_{so} > 2.5$ m s^{-1}. Our experimental trials correspond to V_{so} between 4 and 10 m s^{-1}, for which we always see dip growth, as expected. This criterion corresponds to $We_a > 4$ when rewritten in terms of a modified Weber number $We_a = \rho_a V_{so}^2 d/\sigma$. Unlike the Weber number commonly used in impact problems, We_a depends on the density of air instead of water.

Equation (5.1) also yields an estimate of the local thickness $e_1 = ((\rho_a V_{so}^2 - 2\sigma/d)/2)/\rho\gamma$. A value of $e_1 \approx 75$ μm is obtained based on this expression; see inset of figure 13(*b*). We estimate $e_1/e_0 \simeq 0.5$ and obtain $e_0 \approx 150$ μm, which is the value we adopted for all computational results presented in this work.

Figure 13(*c*) shows the flow visualization below the splash and validates the presence of a strong inward flow, at least of the same magnitude as the splash tip velocity. The relative variation of the horizontal magnitude is in good agreement with our model based on mass conservation, showing in particular a maximum below the dip.

5.2. *Effect of non-dimensional parameters on splash shape*

The modified Weber number We_a reflects the competition between surface tension and aerodynamic suction. Figure 14(*a*) shows a schematic of the expected splash shapes for various We_a. For low We_a, the splash is shorter due to capillary retraction, and flatter because surface tension prevents the bending of the liquid sheet. For larger Weber numbers, the bending becomes more pronounced and the splash shapes reach further.

There are, however, two other effects that the splash shape depends on: drag and gravity. The primary effect of drag is to slow down the splash, in a fairly uniform fashion. One way to estimate the effect of drag on the splash shape is to calculate the relative deceleration of a particle along its trajectory. Let us consider the motion of a slice of splash, of mass $\delta m = \rho e_o d\ell$, travelling at velocity v, over a distance proportional d, and subject to a drag force $\boldsymbol{F}_D = (C_D \rho_a d\ell v^2)/2$. According to Newton's second law of motion, the deceleration can be approximated by $\rho e_o \Delta v/\Delta t = (C_D \rho_a v^2)/2$, which leads to, upon substituting $\Delta t \approx d/v$,

$$\frac{\Delta v}{v} \approx \frac{1}{2} C_D \frac{\rho_a}{\rho} \frac{d}{e_o} = \frac{I}{2}. \tag{5.2}$$

The quantity I is independent of v and thus of the entry velocity V, emphasizing that drag is not responsible for the various degrees of splash bending observed for different entry velocities V. However, the shape of the splash is affected by changing I, either by varying the air–water densities or by changing the dimensions of the wedge. Figure 14(*b*) shows the effect of I on the splash shape. Smaller I (thinner or lighter sheet) produces shorter splashes, without affecting the shape of the splash itself.

Lastly, we redefine a Froude number based on the splash velocity, $Fr_s = V_{so}/\sqrt{gd}$, which reflects the competition between inertia and gravity. Figure 14(*c*) shows that decreasing Fr_s (increasing gravity) induces a global downward motion and tilting of the whole splash. Significant differences are expected starting at $Fr_s = 4$. The experiments presented before are in the range $Fr_s = 7.7$–15, confirming gravity has indeed negligible impact on the splash shapes considered here.

5.3. *Sheet fragmentation*

The strong downward pull locally stretches the water sheet. To estimate the stretching ratio, given the initial sheet thickness that we estimated in the previous section

https://doi.org/10.1017/jfm.2018.273 Published online by Cambridge University Press

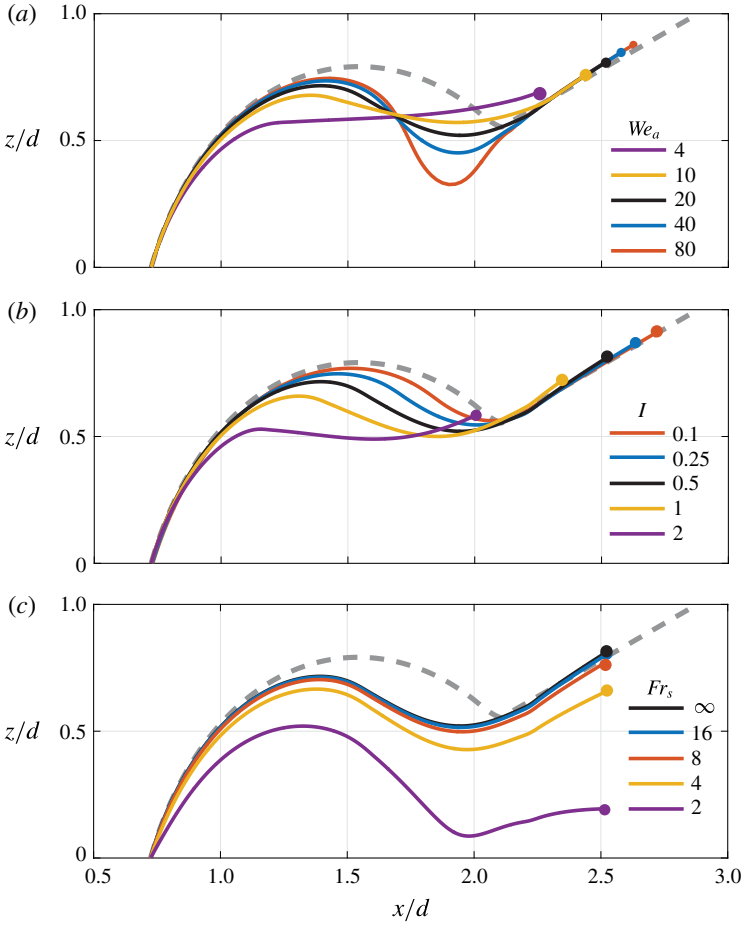


FIGURE 14. (Colour online) Snapshots of the predicted shapes taken at $t^* = 2.5$ showing the effect of the three non-dimensional parameters affecting the splash shape: (*a*) $We_a = \rho_a V_{so}^2 d/\sigma$, (*b*) $I = C_D(\rho_a/\rho)d/e_o$ and (*c*) $Fr_s = V_{so}/\sqrt{gd}$.

($e_o = 150$ μm), we need an estimate of the sheet thickness e_{min} of the splash sheet at its lowest and thinnest point. Fortunately, we have access to e_{min} by observing a spontaneous puncture of the sheet. Figure 15 presents the time sequence of the expansion of a hole in the bottom of the sheet at $t^* \approx 2.5$. The hole expands in all directions at a velocity $V_\sigma = \sqrt{2\sigma/\rho e_{min}}$, known as the Taylor–Culick velocity (Taylor 1959; Culick 1960). We measure $V_\sigma = 5.25 \pm 0.05$ m s^{-1} and calculate $e_{min} = 5.1 \pm 0.3$ μm. This is approximately 30 times smaller than the estimated e_o, in agreement with the maximum stretching ratio of last computable shapes of figure 12(*c*) ($e_{min}/e_o \approx 50$). More importantly, it underlines the dramatic stretching induced by the downward suction. These calculations are the first steps towards developing a low-order model of fragmentation to be pursued in future work.

6. Conclusion

We considered the dynamics of diving wedges. In the first part, we studied the force applied to the wedges during entry. We showed that while sharp wedges

https://doi.org/10.1017/jfm.2018.273 Published online by Cambridge University Press

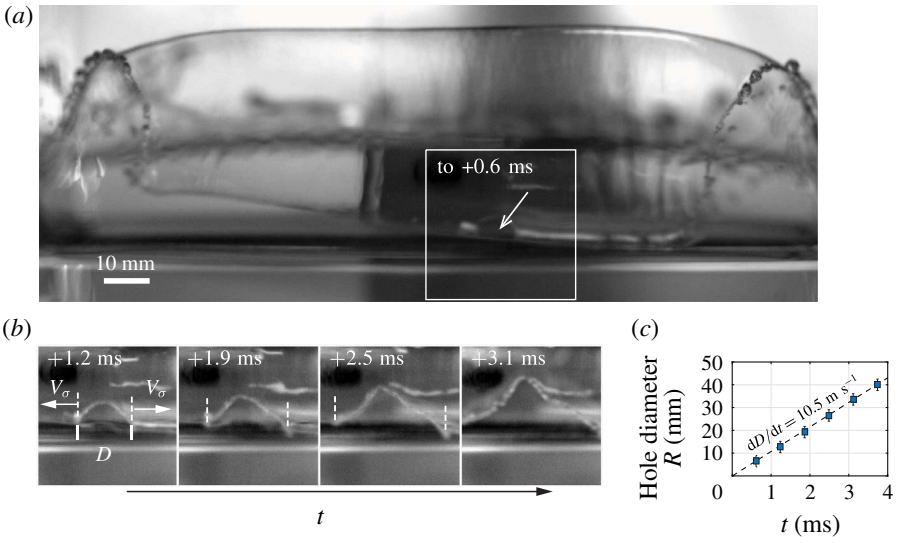


FIGURE 15. (Colour online) (*a*,*b*) Front view of the splash at $t^* \approx 0.85$ for $V = 1.15$ m s^{-1} showing the spontaneous opening of a hole on the thinnest part of the dip. (*c*) The hole expansion velocity is $2V_\sigma$, where $V_\sigma = \sqrt{2\sigma/\rho_a e_{min}}$ is the Taylor–Culick velocity, and provides an indirect measurement of the local sheet thickness $e_{min} \approx 5$ μm, 30 times smaller than the estimated initial sheet thickness e_o.

enter the water smoothly, obtuse wedges experience a large transient peak force before total submersion. The transition between smooth and impactful entry happens for $\alpha \simeq 70°$. Our experimental measurements of the maximum force and the time of occurrence compare well with existing impact force theories (Logvinovich 1972), after incorporating corrections due to the finite aspect ratio L/d of the wedge (Meyerhoff 1970). We also showed that, after submersion, diving wedges are subject to smaller drag forces, approximately two-fold smaller, than the drag forces on immersed wedges. We show that this difference is due to the presence of the cavity, and that the magnitude of the drag is well predicted using existing cavitation theory, even though the origin of the cavity is different.

The second part of this study focused on the dynamics of the splash. We showed that while the entry velocity does not have any noticeable effect on the shape of the cavity, as noted by previous authors (Duclaux *et al.* 2007), it does have a significant effect on the splash shape. Large velocities generally lead to increasingly more ample and further-reaching arabesques. We proposed a one-dimensional model of the splash, incorporating various physical forces acting on the ejected water sheet. We identified a Venturi-suction force caused by the air rushing in between the sheet and the water surface. This phenomenon is similar to the one observed by Thoroddsen *et al.* (2011) for impact of drops in water, but at a much larger scale and smaller velocity, allowing better visualization and seeding. The shape of the splash is driven by competition between Venturi suction that causes the instability of the sheet and surface tension that acts as a stabilizing force. For low-flying splashes, namely those created by large wedge angles, the Venturi suction overcomes surface tension and the splash sheet collapses onto the water surface.

The one-dimensional splash model satisfactorily captures the splash development, but it can be improved in several ways. First and foremost, one can take into account

https://doi.org/10.1017/jfm.2018.273 Published online by Cambridge University Press

the water pile-up under the wedge. The main change would be that the occurrence of full submergence will happen quicker, and as a result, the outermost, straight portion of the splash will be shorter, most likely improving the model's fidelity. To complete this approach, one would have to consider the pressure profile on the wedge to infer the initial conditions given to the water particle until the wedge is fully submerged with respect to the undisturbed surface. Although harder to implement, this method would bridge the gap between the pressure profile and splash shape: the kink in the splash shape would be expected to form shortly after the jet root escapes the wedge's edge, because of the large pressure in this portion of the wetted region.

Another direction to improve the model is to account for the thickness of the splash and its dynamic evolution. Some impact models suggest that the thickness (measured at the jet root) is solely a function of the size and opening angle of the wedge (Pierson 1950), while the thickness scale $\sqrt{\nu D/V_s}$, commonly used in sphere impact problems, includes both splash velocity and viscosity (Thoroddsen *et al.* 2011). Additionally, the thickness is expected to vary slowly along the splash sheet, being thinner at the tip area (excluding the rim), and thicker closer to the base. To our knowledge, little is known about this dependence, especially after the jet root has escaped. A better understanding of the mechanisms governing the splash thickness would form a first step towards developing a fragmentation theory.

Acknowledgements

The work of L.V., T.X., D.Y. and E.K. is partially supported by the National Science Foundation through the NSF CBET grant 1512192 and the Army Research Office through the ARO grant W911NF-16-1-0074 (both to E.K.). E.K. is grateful for sabbatical support from the Center for Computational Biology, Flatiron Institute, Simons Foundation, New York, NY 10010, USA.

Supplementary movies

Supplementary movies are available at https://doi.org/10.1017/jfm.2018.273.

REFERENCES

ABRATE, S. 2011 Hull slamming. *Appl. Mech. Rev.* **64** (6), 060803.

AMADOR, G. J., YAMADA, Y., MCCURLEY, M. & HU, D. L. 2013 Splash-cup plants accelerate raindrops to disperse seeds. *J. R. Soc. Interface* **10** (79), 20120880.

ANDERSEN, A., PESAVENTO, U. & WANG, Z. J. 2005 Unsteady aerodynamics of fluttering and tumbling plates. *J. Fluid Mech.* **541**, 65–90.

ARISTOFF, J. M. & BUSH, J. W. M. 2009 Water entry of small hydrophobic spheres. *J. Fluid Mech.* **619**, 45–78.

BAO, C. M., WU, G. X. & XU, G. D. 2016 Simulation of water entry of a two-dimension finite wedge with flow detachment. *J. Fluid Struct.* **65**, 44–59.

BATTISTIN, D. & IAFRATI, A. 2003 Hydrodynamic loads during water entry of two-dimensional and axisymmetric bodies. *J. Fluids Struct.* **17** (5), 643–664.

BEREZNITSKI, A. 2001 Slamming: the role of hydroelasticity. *Intl Shipbuild. Prog.* **48** (4), 333–351.

BIRKHOFF, G. & ZARANTONELLO, E. H. 1957 *Jets, Wakes and Cavities*. Academic Press.

CALDERER, A., KANS, S. & SOTIROPOULOS, F. 2014 Level set immersed boundary method for coupled simulation or air/water interaction with complex floating structures. *J. Comput. Phys.* **277**, 201–227.

CHANG, B., CROSON, M., STRAKER, L., GART, S., DOVE, C., GERWIN, J. & JUNG, S. 2016 How seabirds plunge-dive without injuries. *Proc. Natl Acad. Sci. USA* **113** (43), 12006–12011.

https://doi.org/10.1017/jfm.2018.273 Published online by Cambridge University Press

CULICK, F. E. C. 1960 Comments on a ruptured soap film. *J. Appl. Phys.* **31** (6), 1128–1129.

DUCLAUX, V., CAILLE, F., DUEZ, C., YBERT, C., BOCQUET, L. & CLANET, C. 2007 Dynamics of transient cavities. *J. Fluid Mech.* **591**, 1–19.

DUEZ, C., YBERT, C., CLANET, C. & BOCQUET, L. 2007 Making a splash with water repellency. *Nat. Phys.* **3** (3), 180–183.

FALTINSEN, O. M. 2005 *Hydrodynamics of High-Speed Marine Vehicles*. Cambridge University Press.

GART, S., CHANG, B., SLAMA, B., GOODNIGHT, R., UM, S. H. & JUNG, S. 2013 Dynamics of squeezing fluids: clapping wet hands. *Phys. Rev.* E **88**, 023007.

GEKLE, S., PETERS, I. R., GORDILLO, J. M., VAN DER MEER, D. & LOHSE, D. 2010 Supersonic air flow due to solid–liquid impact. *Phys. Rev. Lett.* **104**, 0240501.

GHABACHE, E., ANTKOWIAK, A., JOSSERAND, C. & SÉON, T. 2014 On the physics of fizziness: how bubble bursting controls droplets ejection. *Phys. Fluids* **26** (12), 121701.

GILET, T. & BOUROUIBA, L. 2015 Fluid fragmentation shapes rain-induced foliar disease transmission. *J. R. Soc. Interface* **12**, 20141092.

GLASHEEN, J. W. & MCMAHON, T. A. 1996 Vertical entry of disks at low Froude numbers. *Phys. Fluids* **8**, 2078.

GONG, K., LIU, H. & WANG, B. 2009 Water entry of a wedge based on SPH model with an improved boundary treatment. *J. Hydrodyn.* B *(English Ed.)* **21** (6), 750–757.

GORDILLO, J. M., SEVILLA, A., RODRÍGUEZ-RODRÍGUEZ, J. & MARTÍNEZ-BAZÁN, C. 2005 Axisymmetric bubble pinch-off at high Reynolds number. *Phys. Rev. Lett.* **95**, 194501.

GREENHOW, M. 1987 Wedge entry into initially calm water. *Appl. Ocean Res.* **9** (4), 214–223.

HARRISON, S. M., COHEN, R. C. Z., CLEARY, P. W., BARRIS, S. & ROSE, G. 2012 Forces on the body during elite competitive platform diving. In *Ninth International Conference on CFD in the Minerals and Process Industries*. CSIRO.

HOWISON, S. D., HOCKENDON, J. R. & WILSON, S. K. 1991 Incompressible water-entry problems at small deadrise angles. *J. Fluid Mech.* **222**, 215–230.

HSIEH, S. T. & LAUDER, G. V. 2004 Running on water: three-dimensional force generation by basilisk lizards. *Proc. Natl. Acad. Sci.* **101** (48), 16784–16788.

JOUNG, Y. S., GE, Z. & BUIE, C. R. 2017 Bioaerosol generation by raindrops on soil. *Nat. Commun.* **8**, 14668.

VON KÁRMÁN, T. 1929 The impact on sea plane floats during landing. Technical Note 321, 309313. National Advisory Committee for Aeronautics.

KNAPP, R. T., DAILY, J. W. & HAMMITT, F. G. 1970 *Cavitation*. McGraw-Hill.

KOROBKIN, A. A. 1996 Water impact problems in ship hydrodynamics. In *Advances in Marine Hydrodynamics* (ed. M. Ohkusu), vol. 5. Computational Mechanics Publications.

KOROBKIN, A. A. 2001 Water entry of a perforated wedge. In *Proceedings of the 16th Int. Workshop on Water Waves and Floating Bodies* (ed. K. Mori & H. Iwashita). Kazu-hiro Mori.

KOROBKIN, A. A. 2004 Analytical models of water impact. *Eur. J. Appl. Maths* **15**, 821–838.

KOROBKIN, A. A. & PUKHNACHOV, V. V. 1988 Initial stage of water impact. *Annu. Rev. Fluid Mech.* **20**, 159–185.

LHUISSIER, H. & VILLERMAUX, E. 2009 Soap films burst like flapping flags. *Phys. Rev. Lett.* **103**, 054501.

LOGVINOVICH, G. V. 1972 Hydrodynamics of free-boundary flows. *Tech. Rep.* National Advisory Committee for Aeronautics.

MARMOTTANT, P. & VILLERMAUX, E. 2004 Fragmentation of stretched liquid ligaments. *Phys. Fluids* **16**, 2732.

MARSTON, J. O., MANSOOR, M. M., TRUSCOTT, T. T. & THORODDSEN, S. T. 2015 Buckling instability of crown sealing. *Phys. Fluids* **27**, 91112.

MARSTON, J. O., TRUSCOTT, T. T., SPEIRS, N. B., MANSOOR, M. M. & THORODDSEN, S. T. 2016 Crown sealing and buckling instability during water entry of spheres. *J. Fluid Mech.* **794**, 506–529.

MAY, A. 1952 Vertical entry of missiles into water. *J. Appl. Phys.* **23**, 1362–1372.

MAY, A. & WOODHULL, J. C. 1948 Drag coefficients of steel spheres entering water vertically. *J. Appl. Phys.* **19**, 1109–1121.

https://doi.org/10.1017/jfm.2018.273 Published online by Cambridge University Press

MEI, X., LIU, Y. & YUE, D. K. P. 1999 On the water impact of general two-dimensional sections. *Appl. Ocean Res.* **21**, 1–15.

MEYERHOFF, W. K. 1970 Added masses of thin rectangular plates calculated from potential theory. *J. Ship. Res.* **14**, 100–111.

MOFFAT, H. K. 1964 Viscous and resistive eddies near a sharp corner. *J. Fluid Mech.* **18**, 1–18.

PANCIROLI, R., SHAMS, A. & PORFIRI, M. 2015 Experiments on the water entry of curved wedges: high speed imaging and particle image velocimetry. *Ocean Engng* **94**, 213–222.

PARK, S. & RHEE, S. H. 2012 Computational analysis of turbulent super-cavitating flow around a two-dimensional wedge-shaped cavitator geometry. *Comput. Fluids* **70**, 73–85.

PIERSON, J. D. 1950 Stevens Institute of Technology Hoboken NJ experimental towing tank. *Tech. Rep.* 381 Institute of Technology Hoboken, NJ.

QUÉRÉ, D. 2005 Fluid dynamics: impact on Everest. *Nature* **435**, 1168–1169.

ROPERT-COUDERT, Y., GREMILLET, D., RYAN, P., KATO, A., NAITO, Y. & MAHO, Y. L. 1994 Between air and water: the plunge dive of the Cape Gannet *Morus capensis*. *Ibis* **146**, 241–290.

ROSENHEAD, L. 1939 The steady two-dimensional radial flow of viscous fluid between two inclined plane walls. *Proc. R. Soc. Lond.* A **175** (963), 436–467.

SEDDON, C. M. & MOATAMEDI, M. 2006 Review of water entry with applications to aerospace structures. *Intl J. Impact Engng* **32**, 1045–1067.

STENIUS, I., ROSEN, A. & KUTTENKEULER, J. 2006 Explicit FE-modelling of fluid–structure interaction in hull–water impacts. *Intl Shipbuild. Prog.* **53** (2), 103–121.

TAYLOR, G. I. 1959 The dynamics of thin sheets of fluid. Part III. Disintegration of fluid sheets. *Proc. R. Soc. Lond.* A **253**, 313–321.

THORODDSEN, S. T., THOROVAL, M.-J., TAKEHARA, K. & ETOH, T. G. 2011 Droplet splashing by a slingshot mechanism. *Phys. Rev. Lett.* **106**, 034501.

TRUSCOTT, T. T., EPPS, B. P. & BELDEN, J. 2014 Water entry of projectiles. *Annu. Rev. Fluid Mech.* **46**, 355–378.

TRUSCOTT, T. T., EPPS, B. P. & TECHET, A. H. 2012 Unsteady forces on spheres during free-surface water entry. *J. Fluid Mech.* **704**, 173–210.

TRUSCOTT, T. T. & TECHET, A. H. 2009 Water entry of spinning sphere. *J. Fluid Mech.* **625**, 135–165.

TVEITNES, T., FAIRLIE-CLARKE, A. C. & VARYANI, K. 2008 An experimental investigation into the constant velocity water entry of wedge-shaped sections. *Ocean Engng* **35**, 1463–1478.

WAGNER, H. 1932 Über Stoss- und Gleitvorgänge an der Oberfläche von Flussigkeiten. *J. Appl. Maths Mech.* **12** (4), 193–215.

WANG, J., LUGNI, C. & FALTINSEN, O. M. 2015 Experimental and numerical investigation of a freefall wedge vertically entering the water surface. *Appl. Ocean Res.* **51**, 181–203.

WANG, S., LUO, H. B. & SOARES, C. GUEDES 2012 Explicit FE simulation of slamming load on rigid wedge with various deadrise angles during water entry. In *Maritime Engineering and Technology*, pp. 399–406. Taylor & Francis.

WORTHINGTON, A. M. 1908 *A Study of Splashes*. Longmans, Green, and Co.

WU, G. X., SUN, H. & HE, Y. S. 2004 Numerical simulation and experimental study of water entry of a wedge in free fall motion. *J. Fluids Struct.* **19**, 277–289.

XU, L., ZHANG, W. W. & NAGEL, S. R. 2005 Drop splashing on a dry smooth surface. *Phys. Rev. Lett.* **94**, 184505.

YETTOU, E.-M., DESROCHERS, A. & CHAMPOUX, Y. 2006 Experimental study on the water impact of a symmetrical wedge. *Fluid Dyn. Res.* **38**, 47–66.

ZHAO, R. & FALTINSEN, O. 1993 Water entry of two-dimensional bodies. *J. Fluid Mech.* **246**, 593–612.

ZHAO, R., FALTINSEN, O. & AARSNES, J. 1996 Water entry of arbitrary two-dimensional sections with and without flow separation. In *Proc. 21st Symposium on Naval Hydrodynamics*, pp. 408–423. National Academy Press.

https://doi.org/10.1017/jfm.2018.273 Published online by Cambridge University Press